Thor Christian Hobæk

Lessons from Nature

TMM4550 – Nanotechnology, Specialization Project

Trondheim, 16 December 2010

Norwegian University of Science and Technology (NTNU)
Faculty of Engineering Science and Technology (IVT)
Department of Engineering Design and Materials (IPM)

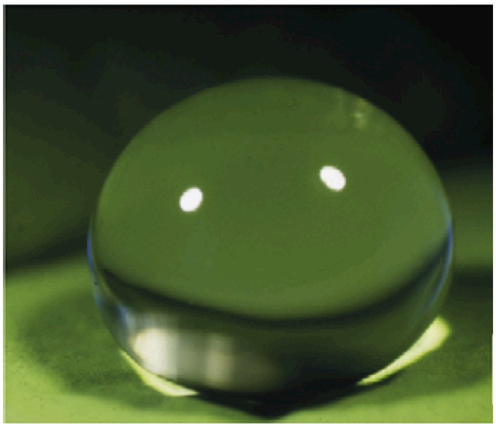

NTNU – Trondheim
Norwegian University of
Science and Technology

Lessons from Nature

Abstract: Lessons from Nature describe the study of processes, structures and designs of living biological systems, which have been formed through evolution. Biomimetics is an important source of inspiration for developing advanced materials. Biological systems often have limited resources available. However, surprisingly good properties are made out of intrinsically weak building blocks, by a hierarchical arrangement of materials from the atomic scale to the macro scale. The huge selection of materials available combined with the recent technological advances, makes engineers able to manipulate material all the way down to the atomic scale.

In this report, an overview of the design of some optimized biological systems will be given, with a special focus on surface properties and the phenomenon of superhydrophobicity. Some of the theoretical models necessary to understand wetting behaviour on surfaces are discussed. It is shown that wetting is dependent both on the surface roughness and the surface chemistry. Inspired by the surface of the lotus leaf, a combination of micro- and nano-scale roughness is a step towards optimization. Furthermore, a short review of methods used to fabricate superhydrophobic surfaces is given, where both advantages and disadvantages are discussed. Some examples will be given of already existing and potential applications. Finally, some thoughts about future work within the field will be discussed, before the conclusion of the project work.

Keywords: biomimetic, lessons from nature, surface, superhydrophobic, wetting, nanotechnology

Lære av Naturen

Sammendrag: Lære av naturen beskriver studier av prosesser, strukturer og design hos levende biologiske systemer som har blitt formet gjennom millioner av år med evolusjon. Naturen er en viktig inspirasjonskilde for utvikling av nye, avanserte materialer. Biologiske systemer har ofte begrenset med tilgjengelige ressurser, men har bygd opp materialet i flere hierarkiske nivåer fra atom-skala og opp til makro-skala, noe som resulterer i fremragende egenskaper. Det enorme utvalget av materialer kombinert med de siste teknologiske nyvinninger, gjør ingeniører i stand til å manipulere materialer helt ned til atom-skala.

I denne rapporten blir det gitt en oversikt over noen optimaliserte biologiske systemer, med spesiell vekt på overflate-egenskaper og fenomenet superhydrofobi. Deretter vil noen av de viktigste teoretiske modellene for superhydrofobi bli diskutert. Det blir bl. a. vist at væting er avhengig av både overflate-struktur og overflate-struktur, og at en kombinasjon av mikro- og nano-skala ruhet er et steg på vei mot optimalisering. Videre blir det vist noen eksempler på metoder for å lage superhydrofobe overflater, hvor både fordeler og ulemper blir diskutert. Deretter blir det en gjennomgang av noen eksisterende og potensielle applikasjoner, før det til slutt blir diskutert videre arbeid og konklusjon fra prosjektarbeidet.

Nøkkelord: bioinspirert, lære av naturen, overflate, superhydrofobi, nanoteknologi

Preface

This report presents the work done during the specialization project (TMM4550, 15 ECTS) given by the Department of Engineering Design and Materials (IPM) at the Faculty of Engineering Science and Technology (IVT). The project work was divided into two phases. The goal of Phase I was to do a broad litterature survey to find interesting functions, properties and structures in nature together with the other master students in the project group, and to define relevant experimental test methods and modelling approaches. Phase II was to be devoted to a more in-depth study of a particular phenomenon, either focusing on theory, experimental, modelling or a mix. This report is therefore divided into chapters corresponding to the progress plan of the project, with the first chapter being a broad litterature review of some interesting biological systems found in nature. After a few weeks of work, the project was narrowed into the field of surfaces, then further down into the phenomenon of superhydrophobicity, inspired by the lotus leaf, the water strider legs and the hairs of the water fern. Thus, the first chapter are mainly focusing on surfaces. The following chapter covers the theory necessary to understand the link between surface structure, chemistry and wetting behaviour. Chapter 3 gives an overview of different approaches to fabricate biomimetic superhydrophobic surfaces, followed by chapter 4 which covers some potential applications. Some thoughts about further work for the master thesis will be discussed in chapter 5. Finally, chapter 6 gives a short conclusion of the contents of this report.

In addition to the specialization project (TMM4550, 15 ECTS) described in this report, I have chosen Bionanotechnology (TFY4525) as my specialization course. This course is divided in two modules; Nanostructuring of surfaces for biological applications (TFYX, 3.75 ECTS), which includes training and practice of techniques in NTNU Nanolab (general cleanroom course, scanning electron microscopy (SEM), general photolithography and surface plasmon resonance (SPR)), and Techniques for Single Molecule Studies (TFY2b, 3.75 ECTS), which involves theory and lab exercises for biophysical microtechniques such as atomic force microscopy (AFM), SEM, transmission electron microscopy (TEM), microarrays and optical tweezers. In addition, I have been following the Nanomechanics course (TKT4146, 7.5 ECTS), where I have learned relevant theory, done nanoindentation lab exercises on the crab exoskeleton and used molecular dynamics with LAMMPS to study the mechanical behaviour of single crystal compared to nanocrystalline Si and metallic nanorods. The three reports written in this course have been included in the appendix. Furthermore, I have completed training for AFM and focused ion beam (FIB) at the NTNU Nanolab beside the curriculum.

Before introducing the reader to the contents of this report, I would like to thank my supervisor, Professor Christian Thaulow for counseling, ideas and inspiring discussions and group meetings. Furhtermore, I would like to thank two of his PhD students Christer Honoré Ersland and Bjørn Rune Rogne for helping with the atomistic modelling in LAMMPS and arranging the FIB training course, respectively. Finally, thanks to my fellow master students in the project group; Kristian Greger Leinan, Robin Hansen Brenden, Eirik Stavik Rønning and Jørn Hwan Kraavik Skogsrud for useful inputs during the project work.

Problem text

THE NORWEGIAN UNIVERSITY
OF SCIENCE AND TECHNOLOGY
DEPARTMENT OF ENGINEERING DESIGN
AND MATERIALS

PROJECT WORK AUTUMN 2010
FOR
STUD.TECHN.
THOR CHRISTIAN HOBÆK

LESSONS FROM NATURE

Lære av naturen

Nature has gone through evolution over the 3.8 Gyr since life is estimated to have appeared on the Earth and biologically inspired design from nature is referred to as ‘biomimetics’. Biological materials are highly organized from the molecular to the nanoscale, microscale and macroscale, often in a hierarchical manner with intricate nanoarchitecture that ultimately makes up a myriad of different functional elements.

This project work is focused on the atomistic bottom-up multiscale analysis of the fracture of geometries found in biological and bio-inspired nanocrystals and to develop biomimetic materials with light weight, high stiffness, high strength and large tolerances to damage.

One example is sea sponges, with a fossil record that dates back more than 0.5Gyr. This organism consists of a biomineralized hierarchical nanostructure of silica and organic interlayers, with characteristic structures across multiple length-scales from macroscale to nanoscale. Even though the basic constituents are intrinsically highly brittle, the overall hierarchical structure is not (actually you can jump on the sponge without recording failure).

The modeling challenges will be development of models on the atomistic level and linking the results to macroscopic response. Experiments in NTNU NanoLab will be needed to calibrate and confirm the modeling approach.

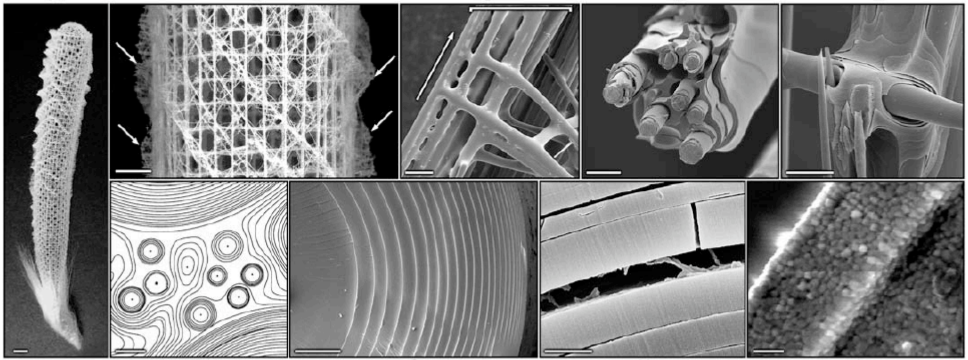

Hierarchical biological silica-based structures, here deep sea sponge *Euplectella*

The project is divided in two phases. During the first phase the four students work together to establish the basic knowledge of atomistic and multiscale modeling and testing of bio-inspired materials. This includes a broad literature survey, definition of interesting biological systems and properties, atomistic modelling approaches (including software packages, interatomic potentials and simulation procedures) and nanomechcanical testing approaches. At the end of Phase 1, tentatively October 11th, the students arrange a seminar where the results are presented and each student present their specialization direction, including aims/objective and a detailed progress plan with time schedule. Phase 2 is very open, and can be atomistic calculations on the supercomputer at NTNU (Njord), testing at NTNU NanoLab or NanomechanicalLab, theoretical, literature in-depth study or all kind of combinations.

During evaluation of the project report it is emphasized if the problem addressed by the student is presented clearly, if the report is well elaborated, and to what extent a personal presentation of the topic is given based on the students own judgement.

The report shall include the given problem text and shall have a list of contents. In the preface of the report the candidate should specify actual courses (fordypningsemne) chosen within his/hers specialization. Actual problems to be addressed in the project are to be stated in the beginning of the report and briefly discussed. In the beginning there should also be a summary of important results and a conclusion. The report should not exceed thirty pages inclusive of illustrations and sketches included in the text.

Additional tables, drawings, detailed sketches, photographs, etc. are to be included in an appendix part at the end of the thirty pages report. In the main report, at appropriate places, it should be referred to the appendix part to specify where additional information is given there. However, the main report should be so formulated that it can be read and understood without checking the Appendix.

Figures and tables should be complete with necessary text. Literature references should be indicated by means of a number in brackets in the text, and each reference should be further specified at the end of the report in a reference list. References should be specified with name of author(s) and book, title and year of publication, and page number.

Three weeks after project start, an A3 page describing the planned work should be made. It should be handed over to the institute as paper version including electronic version as a pdf-file. A template for this sheet is found on IPM’s web-page, using the link http://www.ntnu.no/ipm/studier/undervisning.

Not later than 3 weeks before deadline of the final project report, an A3 page summarizing and illustrating results obtained in the project work, should be handed in (paper and electronically version).

The projects are presented orally by the students on the 21st of October 2010. Participation during the presentation is compulsory for all project students.

Official deadline for the delivery of the report is 21st of December 2010 according to the university plan for the study. The report should be delivered in two paper copies and one electronic version on a CD or DVD.

Contact persons:
At the department : Christer H Ersland, Inga Ringdalen Vatne and Bjørn Rune Rogne
University of Oslo : Hans Petter Leinaas
At SINTEF : Erling Østby
From the industry : Morten Karslsen, Statoil Forskningssenter, Rotvoll

Christian Thaulow
Supervisor

Contents

List of Figures

Glossary

A area.

f_{LG} fraction of the liquid-gas interface under the droplet.

f_{SL} fraction of the solid-liquid interface under the droplet.

H height.

H_{cr} critical height.

l length.

M_w molecular weight.

n refractive index.

p_c critical pressure.

r roughness factor.

r_f roughness factor of wetted area.

U potential energy.

α sliding angle.

η slenderness ratio.

η_e equi-energy slenderness ratio.

γ surface free energy, surface tension.

γ_{LG} surface tension of the liquid-gas interface.

γ_{SG} surface tension of the solid-gas interface.

γ_{SL} surface tension of the solid-liquid interface.

Π_D disjoining pressure.

θ apparent contact angle for a rough surface.

θ_0 contact angle for a smooth surface.

θ_{adv} advancing contact angle.

θ_{rec} receding contact angle.

Acronyms

AFM atomic force microscopy.

CAH contact angle hysteresis.

CNT carbon nanotube.

CVD chemical vapor deposition.

FIB focused ion beam.

NIL nanoimprint lithography.

NMR nuclear magnetic resonance.

PDMS polydimethylsiloxane.

PECVD plasma-enhanced chemical vapor deposition.

SEM scanning electron microscopy.

SPR surface plasmon resonance.

TEM transmission electron microscopy.

TNIL thermal nanoimprint lithography.

UV-NIL UV nanoimprint lithography.

Chapter 1

Biological materials

For millions of years, life on earth has developed through evolution. According to the expression "survival of the fittest" used by Charles Darwin, the most successful species is defined as those being able to adapt to the environmental changes during this planets lifespan. Therefore, many of the structures and functions we find by studying nature is a result of the most optimum strategy for dealing with the various challenges of life. Nature has been and still is a great source of inspiration for solving challenges within the field of engineering. In this chapter, some interesting biological functions will be presented as a background material for the fabrication as well as the chapter on applications later in this report.

1.1 Dealing with deformation

Crustaceans form a very large group of arthropods, which include animals such as lobster, crabs, crayfish, krill, shrimp and barnacles. They posses an exoskeleton that stabilizes the whole body and serves as a protection mechanism against predator attacks. The exoskeleton is a composite material consisting of an organic matrix, mostly α-chitin, and inorganic minerals, mostly calcium carbonate. The composite material optimize mechanical strength for protection and flexibility for movement through evolution. The amount of mineralization is an important parameter, because it decides which of the two properties that are the most crucial. Lobsters and crabs are two animals that have adopted different strategies for survival. The American lobster (*Homarus Americanus*) is a fast-swimming animal that tries to escape from its predators, while the crab (*Cancer Pagurus*) is more stationary and clings to the ground. The lobster therefore needs flexibility more than it needs mechanical strength, thus its exoskeleton has a lower mineral content, while the case is the opposite for the crab [2].

Raabe et. al. [3] analysed the micro-structure of the exoskeleton and found a structural hierarchy from the atomic scale to the macroscopic scale. A schematic of this structure is shown in Figure 1.1. Polysaccharide molecules (I) (N-acetyl-glucosamine) form polymer chains of α-chitin (II), which are arranged anti-parallel to form nano-fibrils wrapped with proteins (III). These nano-fibrils form clusters of chitin-protein fibres embedded in a mineral-protein matrix (IV). In the cuticle, the tissue forms planes with a honeycomb-like structure (V), which are gradually rotated around the normal axis of the cuticle in a twisted plywood (VI). The macroscopic scale (VII) consists of three layers from the outer to the inner surface; the epicuticle, the exocuticle and the endocuticle. The epicuticle is a thin waxy layer, which has the property of being waterproof. It is the exocuticle (thickness about $200 - 300$ μm) and the endocuticle (thickness about $250 - 2500$ μm), which are responsible for the mechanical strength of the exoskeleton. The exocuticle displays a higher

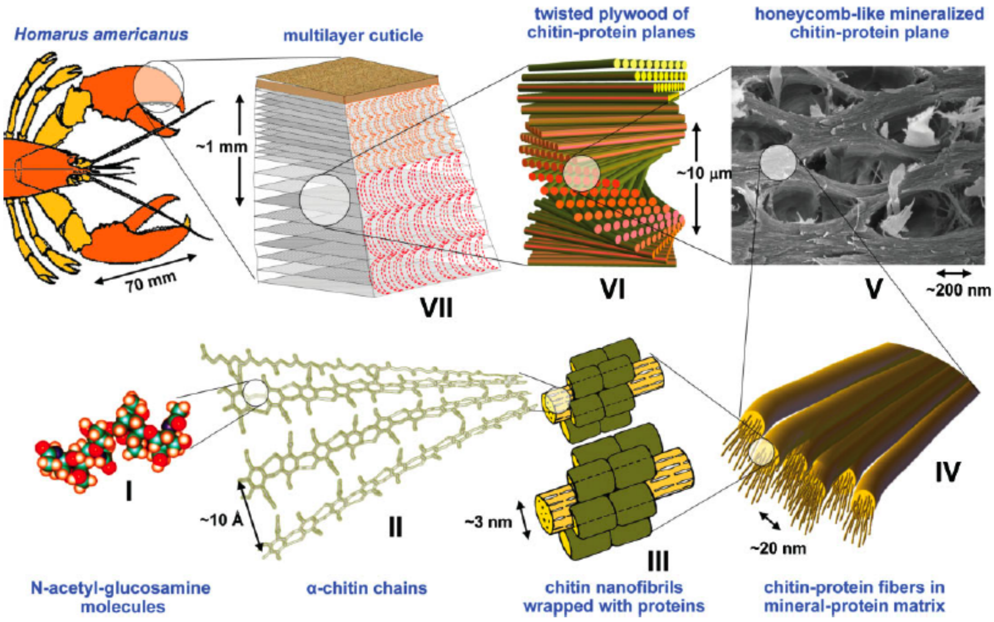

Figure 1.1: Schematic showing the hierarchical structure of lobster cuticle from the atomic scale up to the macro scale [1]

mineral content, smaller canal pores and higher stacking density of the twisted plywood layer, compared to the endocuticle. This leads to a larger hardness and elastic modulus of the outer layer, verified by micro- and nano-indentation experiments [3].

The effect of arranging the exoskeleton into two compartments; a hard layer facing the exterior surface followed by a softer layer, is to avoid catastrophic failure. A hard and stiff material can deal with high loads without significant deformation. However, if the force reaches a certain level, cracks will be initiated and propagate fast, leading to complete fracture. With the arrangement of the lobster cuticle, the softer layer absorbs most of the deformation energy without fracture of the outer layer. Similar arrangements can also be found in the morphology of teeth, which have a hard, brittle outer layer (enamel) followed by a softer layer (dentin) [4], and in armoured fish (*Polypterus senegalus*), which has layered exoskeleton with gradually decreasing hardness and stiffness [5]. The purpose is the same as for lobster cuticle; to avoid catastrophic failure of the material.

1.2 Anti-reflection

Moths and butterflies are closely related insects, which have developed an anti-reflective surface on their eyes. The eyes have a hierarchical structure on the micro- and nano-scale (see figure 1.2), with the surface of the convex eye covered by an array of nipple-shaped protuberances arranged in a hexagonal lattice structure, called facet lenses. The nipple height varies between different species, ranging from about $50 - 250$ nm [6]. For the European peacock (*Inachis io*) shown in figure 1.2, the diameter of the facet lens is about 23 μm, while the height and the nearest-neighbour distance of the nipples is about 200 nm and 210 nm respectively. The nipples reduce the reflectance from 4% to 1% compared to a smooth facet lens with no surface structure [7]. Although this change may seem minor and insignificant, it reduces glare during daylight and moonlight, making the insect less detectable by predators. Besides the camouflage effect, it may also enhance vision of the butterfly when it flies during the night, as transmission of light increase with decreasing reflectance. Also, some moth species (*Cephonodes hylas*) have developed a similar nipple array on their wings as well [8]. This reduces the visibility of the insect further.

The mechanism behind reducing the light reflectance is that the nipples act as a gradient in the effective refractive index from air ($n = 1$) to the facet lens medium ($n = 1.52$), because the size and the distance between the nipples are lower than the wavelength of light. The nipple array behaves as a gradient-index film on a flat substrate, where the refractive index varies continuously from the surrounding medium to the underlying substrate. The effective refractive index of a composite layer can be calculated by

$$n_{eff} = [n_s^2 f + n_{air}^2(1 - f)]^{1/2} \tag{1.1}$$

where n_s, n_{air} and f is the refractive index of the underlying substrate, the refractive index of air and a filling factor [9]. Because f is gradually changing due to the nipple structure, the effective refractive index is also gradually changing. The reflectance from the surface depends on the size and shape of the nipple geometry. Optical modelling showed that the highest reduction in reflectance was achieved by the tallest (250 nm), paraboloid-shaped nipples, which nearly touches each other at the base [6]. The anti-reflection / anti-glare properties of the eyes and wings of the moth have a great potential for producing new biomimetic coatings.

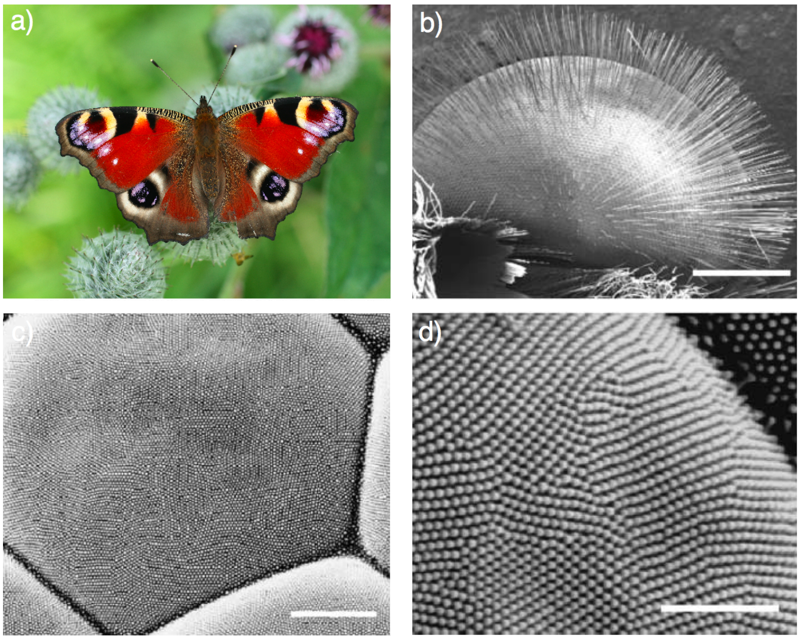

Figure 1.2: a) Image of the whole European peacock (*Inachis io*). b) SEM-image of the complete eye (scalebar = 500 μm. c) Hexagonal facet lens with a superimposed array of nipples (scalebar = 5 μm). d) Highly ordered array of nipples (scalebar = 2 μm) [6].

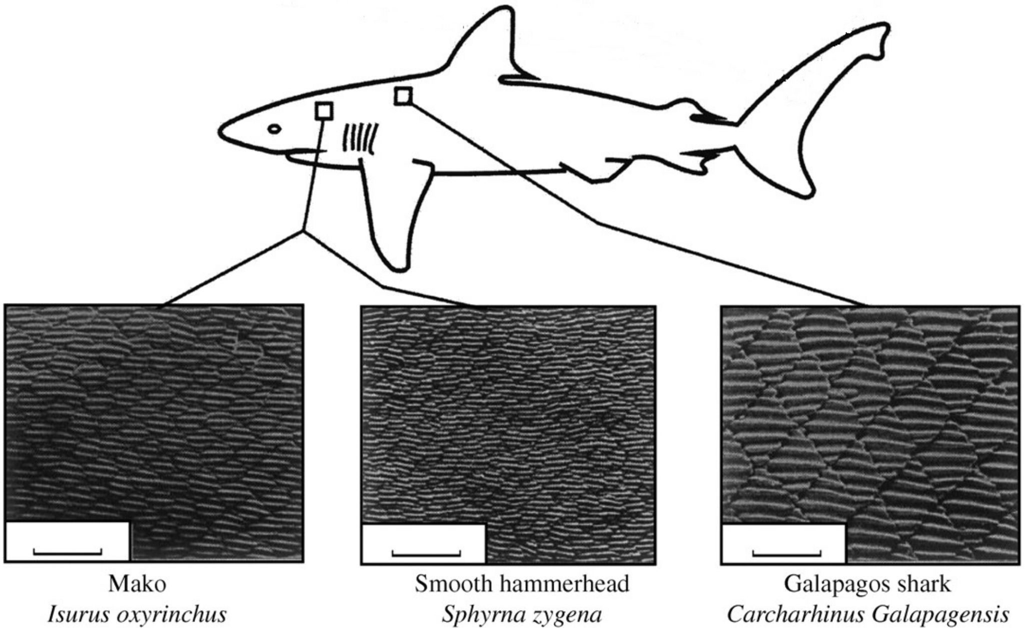

Figure 1.3: Micro-scale structures on the surface of the shark skin reduces the fluid drag and enables more efficient swimming (adapted from [11]).

1.3 Fluid drag reduction

The skin of the fast swimming shark is a multifunctional material in the sense that it protects against biofouling and reduces the fluid drag as it swims through water. The surface of the skin is covered by tiny ridges on the micro-scale (see figure 1.3) that are aligned parallel to the direction of flow. It has been shown that the appearance of ridges reduces the drag by 9.9 % compared to that of a smooth surface [10].

The drag on an object is a measure of the energy required to displace fluid in front of the object to behind it. When sharks swim through water, the fluid behaves as a turbulent medium due to the large length scale of the animal. For complete turbulent flow, the fluid velocity distribution exhibits complete randomness. However, in this case, the fluid close to the surface (viscous sub-layer) is organized to a certain degree [11]. The fluid behaviour in the viscous sub-layer is dominated by vortices that rotate around the axis of the mean velocity direction (streamwise vortices), which is in the direction of the swimming. Interaction between the vortices and the surface can cause sudden bursts of vortices ejected out from the surface. This phenomenon is responsible for a large part of the fluid drag, therefore reducing the bursting of vortices is critical in the strategy of achieving drag-reduction [11].

Fluid drag increases with increasing surface area due to shear stresses. In shark skin however, the surface is structured so that the vortices form above the ridges, so that higher shear-stress only occurs localized at the top of these ridges. In the valleys below, very low shear stresses are involved. Thus, the effect of the ridge-like surface structure is to reduce the fluid drag by localization of vortices, despite the fact that a larger surface area is introduced.

Figure 1.4: (a,b) The sand fish skink is able to move in a swimming-like fashion in the sand of desert dunes [15, 12]. (c) The low friction between the sand fish skin and the sand is partially responsible for this movement [13].

1.4 Solid friction reduction

The sand fish skink (*Scincus scincus*) is a lizard that has adapted an underground existence underneath the sand dunes in the deserts of Northern Africa and the Arabian Peninsula. It is able to move through the sand in a swimming-like fashion with velocities up to 30 cm/s at a depth of 15 cm, with a very low friction and high abrasion resistance against sand [12]. Work by Reichenberg et. al. showed that the friction angle θ (the inclined angle of a surface when the sand grains starts to slide) is lower for the skin of the sand fish skink ($\theta = 21°$) than for other technical materials like Teflon ($\theta = 36°$), glass ($\theta = 28°$) and steel ($\theta = 25°$) [13].

The low friction is due to the scales on the skin surface. The skink's scales are covered by long ridges with a height of around 250 nm and an inter-ridge separation distance of about 5 μm [14]. The scales consists of glycosylated keratins with a high amount of sulphur. Glycosylation of the surface lead to an almost completely absent attractive force between the scale surface and a silicon AFM tip [14]. Thus, it is suggested that it is the chemical composition of the nano-scale ridges on the scale surface that is responsible for the low surface adhesion. Also, the locomotion of the skink in sand has been investigated using nuclear magnetic resonance (NMR) imaging [12]. The movement of the sand fish leads to local decompaction of the sand surrounding the lizard (making the sand less compact). This makes the sand behave as a viscous fluid, enabling the lizard to "swim" using its hind limbs.

1.5 Reversible adhesion in nature

Many examples where adhesion plays a decisive functional role can be found in nature. Among them are flies and ants walking in the ceiling, carnivorous plants like the sundew (*Drosera*) and the spider's silk, which uses adhesion as a strategy to catch its prey. One of the most studied examples however, is the tokay gecko (*Gecko gecko*) that has its natural habitat in the rainforests of South-east Asia. It has the remarkable ability to climb vertical surfaces at velocities higher than 1 m/s, with strong attachment to the surface and easy detachment for rapid movement [16].

Characterization of the surface of the gecko's toe has revealed that it is covered by stiff hair-like setae primarily made out of beta-keratin [18]. The setae are about 110 μm in length and 4.2 μm in diameter, distributed on a ridge-like array on each toe with a

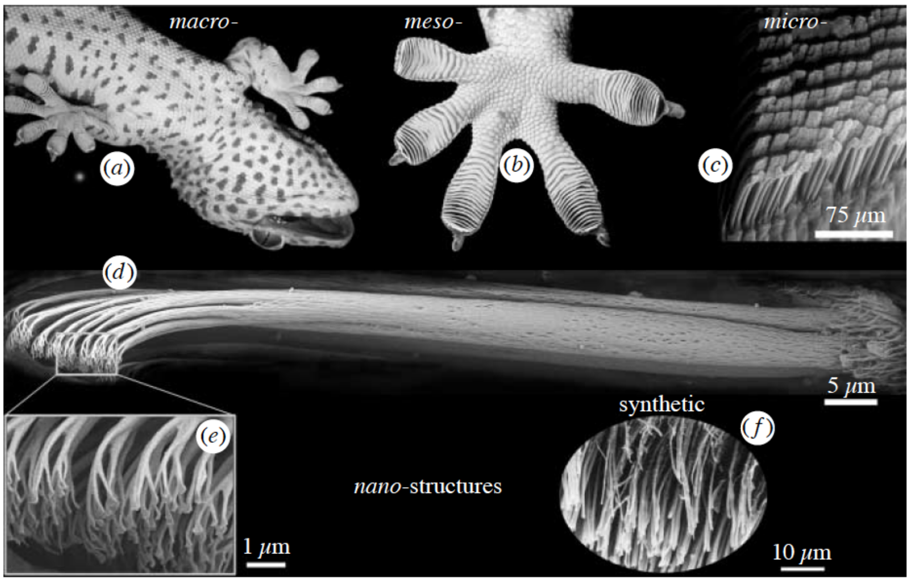

Figure 1.5: (a) The tokay gecko seen from below. (b) The surface of the toes have an array of lamellae covered with setae on the micro-scale (c). (d,e) SEM microgram of a single seta shows branching to hundreds of spatulae. (f) The structure of these nano-scale spatulae have inspired engineers to develop biomimetic adhesives of synthetic polyimide [16, 17].

density of about 14 400 setae per mm^2 [19]. Furthermore, the setae branches to an array of hundreds of smaller hairs called spatulae. The spatulae have a triangular flat end and are about 0.2 μm in length and diameter. Thus, the surface structure of the gecko's feet is hierarchical from the macro to the nano-scale (see figure 1.5), which is able to conform to the local roughness of the underlying surface it attaches to.

The mechanism behind the attachment of the gecko's feet is quite fascinating. When the setae approach the surface, they are oriented in a fashion similar to that shown in figure 1.5. The gecko applies a pre-load so that each of the setae conform properly to the surface using the spatulae ends. During this pre-load, the spatulae straightens out so that their ends become oriented perpendicular to the surface [16]. The push on the surface is accompanied by a drag parallel to the surface, in order to achieve attachment. This places the setae under tension, creating a large frictional force which is sufficient to attach the gecko to the surface. Experiments showed that the two front feet of a gecko supports a force of 20.1 N parallel to the surface before slip occurs [20]. Other experiments showed that when a single setae is properly attached, it can generate a 40 μN adhesion force [21]. If all the 6.5 million setae of a 50 g tokay gecko were attached simultaneously, this would provide a total adhesive force of 1300 N, enough to support the body weight of two human beings [22, 20]. Thus, the gecko needs only to attach about 0.04% of its setae to support its own body weight. It may seem that the adhesive ability of the gecko is greatly exaggerated. One need however to consider that not all of the setae may be able to attach simultaneously. Also, high surface roughness or dust could mean that a large fraction of the setae are not able to attach properly. Thus, the adhesive properties of the gecko's feet are very robust.

One can wonder how the gecko manages to detach from the surface when such high adhesion forces are involved, using only 15 ms [16]. This mechanism is as interesting as the mechanism of attachment. By increasing the angle the setal shaft makes with the surface to about 30° [23], the foot is essentially peeled off like a piece of tape adhesive. This peeling motion makes sure that only a small fraction of setae detach at any instant, thus reducing the required force.

Although the gecko has been studied for decades, it was long unclear what mechanisms were involved in the strong adhesive force. Among the possible mechanisms that have been proposed are suction, friction, static electricity, secretion of glue, capillary forces and van der Waals forces [22]. All but the latter two mechanisms were rejected by the end of the 1960s [16].

To determine whether capillary forces or van der Waals forces were responsible for the adhesion of the setae, friction and adhesion were measured between a live gecko's toe and two smooth surfaces; a hydrophilic SiO_2 and a hydrophobic GaAs wafer [23]. If capillary adhesion were dominant, it would be expected that the adhesion towards the hydrophobic surface should be much less than the hydrophilic. There was however no significant difference in the measured adhesion between the two surfaces. Autumn et. al. [23] also found that the gecko's setae were strongly hydrophobic. As only van der Waals forces can cause two hydrophobic surfaces to adhere in air [24], the experiment proved that this mechanism could sufficiently describe the excellent adhesion of the gecko's feet.

1.6 Water collection

Creatures living in hot and arid areas are challenged by the shortage of water. Because water is the universal prerequisite for life as we know it, nature has come up with a clever design through evolution that deals with this problem. One example is the Namib Desert Beetle (*Stenocara gracilipes*), which collects water during the morning when the air humidity is high [25]. The size of the fog droplets are only about $1 - 40\ \mu$m in diameter, so they are easily carried away by the wind. To collect water, the beetle brings its back to a tilt by raising its hind legs, so that the humid air impacts the beetle's back. The surface structure of the beetle's back are bumpy, consisting of alternating wax-coated, hydrophobic areas and hydrophilic non-waxy regions at the peak of the bumps. The bumps are about 500 μm in diameter, separated by a distance of $500 - 1500\ \mu$m. The hydrophilic regions have a smooth surface, whereas the hydrophobic regions have protuberances shaped as hemispheres with 10 μm in diameter, placed in an hexagonal array [25].

Figure 1.6: The Namib Desert Beetle with its back covered by alternating hydrophobic and hydrophilic regions [25].

The hydrophilic regions act as seeding points where the water condense. As water condense from the humid air, it forms droplets that will increase in size over time. Eventually, the droplets reach a size when the capillary forces attaching the droplet to the surface is overcome by the gravity and the force experienced by the wind. The droplet is then detached and starts rolling over the hydrophobic areas towards the beetle's mouth, where it is consumed.

1.7 Water-floating

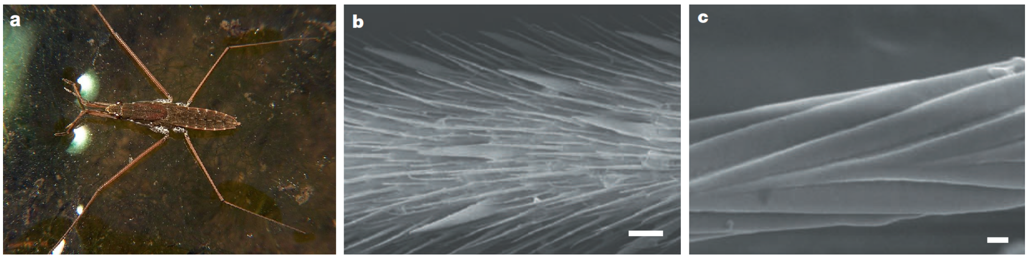

Figure 1.7: (a) A water strider floating on top of water without breaking the surface. (b) Scanning electron micrograph of the water strider leg covered by microsetae (scale bar = 20 μm). (c) Nano-grooves on the surface of a microsetae (scale bar = 200 nm) [26]

Some insects like the water strider have the ability to stay floating and walk efficiently on top of water. Even when large raindrops disturb the water close to the water strider, it simply bounces away and stays floating. It was previously thought that this effect was due to secreted hydrophobic waxes. However, it is the hierarchical structure of the water strider's legs that results in the extreme water resistance [26]. The legs are covered by a large number of oriented tiny hairs called microsetae, inclined by an angle of about 20°from the surface of the leg, and with a diameter that range from typically hundreds of nanometres to about 3 μm and a length of about 50 μm. Each microsetae are further covered by fine nano-grooves on the surface, which traps air underneath the water surface. As will be discussed in later sections, trapping of air in nano-structures assists in water-repellency. From previous experiments, it was found that the legs were able to support a weight of about 15 times the total body weight of the insect before breaking the water interface [26]. At that point, the volume of displaced water was about 300 times that of the leg itself. Thus, the legs of the water strider show a strong water-repellency due to its hierarchical surface structure.

A similar strategy found in nature for staying afloat, is exhibited by the water fern plant (*Salvinia*). When submerged under water, the leaf's surface shows a silvery reflection, resulting from trapped air bubbles. Actually, the water fern is able to retain an air film under water for 17 days [27]. The hierarchical surface of the *Salvinia* is made of multicellular hair structures covered by hydrophobic waxes on the nano-scale. The hairs branch into four smaller multicellular hairs at the end, which eventually merge together and form a flat patch at the very end [28]. What is remarkable with this structure is that while most of the hairs are covered with waxes that make them superhydrophobic, the patch ends display a smooth, hydrophilic surface with no wax crystals superimposed. Thus, about 2% of the otherwise superhydrophobic leaf surface are hydrophilic.

As can be seen from figure 1.8, droplets form a nearly spherical shape, resting on top of the hairy structures, while higher magnification shows the meniscus between the droplet and the patched end. The sample were obtained by freezing fresh leaves with droplets of water-glycerol solution dispersed, and imaging with a low-temperature SEM [28]. The effect of having hydrophilic patches at the hair ends is that the water sticks, while the waiter-air interface is prevented to penetrate the hairy structure, due to the superhydrophobicity. It can be seen that the hairs bend and swing back when the hairs detach from the droplet [28].

The purpose of having hydrophilic patches are probably to stabilize the water-air interface when pressure fluctuations occur under water, due to turbulent flow. Flow experiments showed that the distance between the interface and the leaf base varied due to the oscillations. To retain the air film at the surface, the energy required for the water to penetrate between the hairs have to be maximized. Thus, the hairs are formed so that they give a large increase in the surface energy within a small height difference, resulting that the water-air interface cannot come much closer to the leaf base due to the rapid increase of energy. On the other hand, because the water is pinned to the hydrophilic ends of the hairs, energy is required to remove the interface layer far away from the surface. Thus, the hierarchical arrangement and surface chemistry of the water ferns contributes to maintain a stable air film at the surface, even when fluctuating pressures are present. This mechanism can be exploited for drag reduction under water, as will be discussed in section 4.4.

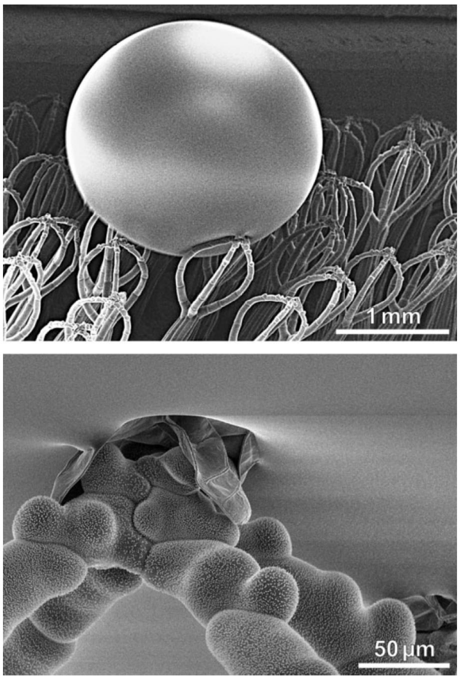

Figure 1.8: The surface of the water fern consists of superhydrophobic multicellular hairs with hydrophilic patch ends, which sticks to water (adapted from [28]).

1.8 Self-cleaning and anti-adhesion

Some plants growing in wet environments, such as marshland, exhibit self-cleaning and anti-adhesive functions. One of them is the Lotus flower (*Nelumbo nucifera*), which has been a symbol of purity in Asian traditions for at least 2000 years [29]. Even when emerging from muddy waters, it stays unaffected by pollution. The surface structure, along with the chemical composition of the outermost layer, the cuticle, is responsible for this effect. The surface is said to be superhydrophobic, because water droplets forming at the surface assume a nearly spherical shape (contact angle about 160°) and will start rolling off by inclining the surface plane by only 4°. The self-cleaning of the lotus leaf is independent of the chemical composition of adhered particles, and it functions as a defence mechanism against potentially dangerous plant pathogens, such as bacteria and fungi. In addition, it

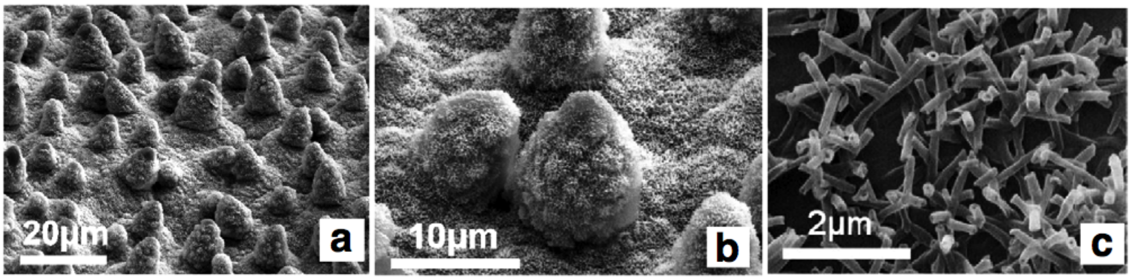

Figure 1.9: (a) SEM micrographs of irregularly arranged papilla shaped cells on the surface of a Lotus leaf. (b) Single cells with a superimposed layer of hydrophobic waxes. (c) Three-dimensional wax tubules with a random orientation [30]

is important to keep the surface dry, especially in humid environments, as diffusion of CO_2 necessary for the photosynthesis, is 10.000 times slower through water than air. Thus, it is critical to avoid formation of water films at the leaf's surface.

Surface roughness at two hierarchical scales leads to a superhydrophobic surface with a very high contact angle. The surface structure consists of convex papilla shaped cells (aspect ratio $\beta < 3/2$ and $> 1/2$) with a superimposed layer of three-dimensional crystal waxes. The hierarchical structure is shown in figure 1.9. The papilose cells are distributed randomly across the surface of the leaf, with variations in height and distance separating individual cells. The wax crystals form hollow structures, called tubules. They contain a high amount of nonacosan-10-ol, which is a secondary alcohol with a low surface energy. The tubules are typically $0.3 - 1.1$ μm in length and $0.2 - 0.3$ μm in diameter [29].

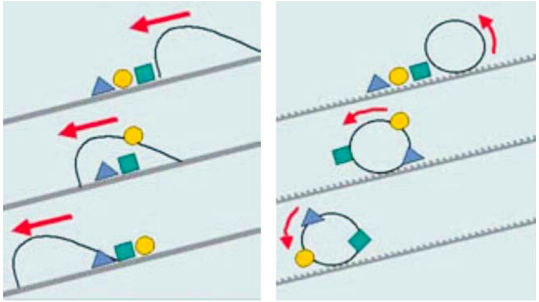

Figure 1.10: Diagram illustrating the mechanism behind self-cleaning on a micro-structured surface, compared to that of a smooth one [31].

Because of the hierarchical surface structure, air becomes trapped in the cavities between the convex cells, which leads to an increase in the water-air interface area and a corresponding decrease in the solid-water interface. Due to the low surface energy, it is energetically favourable to form a small contact area with the surface, so that the adhesive force is reduced. Similarly, a pollutant particle on the lotus leaf surface is practically sitting on a bed of nails, which means that it has a very low contact area. Because of the reduced contact area and the low surface energy, only weak van der Waals forces bind the particle to the surface [32]. The adhesive force between the particle and the surface is lower than the the capillary attraction forces from a rolling water droplet, so it is easily removed from the leaf's surface.

This effect is illustrated in figure 1.10 for a water droplet interacting with dust particles on a smooth surface and a surface with micro-roughness. The droplet rolls off the surface when it is tilted. However, while the droplet only redistributes the dust particles on a smooth surface, it carries them away on the micro-textured surface. Thus, the surface of the lotus leaf has been used as a source of inspiration for various applications, discussed in chapter 4.

Chapter 2

Wetting theory

Wetting theory is the theory describing the intermolecular interactions when a liquid is brought into contact with a solid surface. The degree of wetting is determined by the force balance between adhesive and cohesive forces. The theory is important in order to understand the mechanics behind surface behaviour involved in the examples discussed in the previous chapter. Terms like surface tension, surface energy, contact angles, contact angle hysteresis, hydrophobicity, hydrophilicity and the effect multi-scale roughness has on wetting properties will be discussed in this chapter.

2.1 Surface tension and contact angles

2.1.1 Surface tension

Surface tension, represented by the symbol γ, has two equivalent definitions in physics, one definition is in terms of force, the other in terms of energy. The first definition is that surface tension is a force, which acts perpendicular and inward from a boundary of any surface or interface. This can be visualized by imagining a needle floating on the surface of water, see figure 2.1. The weight of the needle is balanced by a surface tension force given as

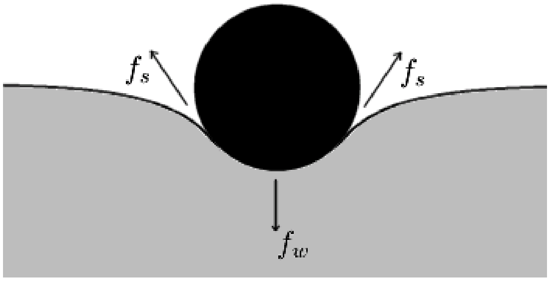

Figure 2.1: Cross-sectional diagram showing the balance of the gravitational and the surface tension force acting on the needle.

$$f_s = 2\gamma l \tag{2.1}$$

where l is the contact length of the water-needle interface (the factor of 2 is because the needle have two sides). The surface tension is therefore measured in force per unit length (N/m).

The other definition is thermodynamical in the terms of the work per unit area (J/m^2) required to produce a new surface, given by

$$\delta w = -\gamma dA \tag{2.2}$$

where a decrease in A (negative dA) corresponds to work done by the system, whereas an increase in surface area (positive dA) requires work to be done on the system. The work corresponds to Gibbs free energy for a non-expansive process (with constant pressure and volume) in a closed system [33]. Thus, the thermodynamic definition of surface tension is given by

$$\gamma = \left(\frac{\partial G}{\partial A}\right)_{T,p} \tag{2.3}$$

The effect of surface tension is therefore to decrease the surface area between gas, solid or liquid, because thermodynamics requires any spontaneous process to be accompanied by a decrease in Gibbs free energy.

2.1.2 Wetting on smooth surfaces

The contact angle is defined as the angle at which a liquid/gas interface meets a solid interface (often called the triple line [34]). Consider a drop of liquid placed on a perfectly smooth solid surface. The contact angle θ_0 is related to surface tension by Young's relation (sometimes also called the Young-Dupré equation) [33]

$$\cos\theta_0 = \frac{\gamma_{SG} - \gamma_{SL}}{\gamma_{LG}} \tag{2.4}$$

where γ_{SG}, γ_{SL} and γ_{LG} is the surface tension of the solid-gas, solid-liquid and liquid-gas interface respectively. The equation represents the force balance of adhesive and cohesive forces, which acts between the three different phases. Adhesive forces between a water droplet and a solid surface will cause the droplet to spread out, making as large contact area as possible. Cohesive forces will try to minimize the water-solid interface area. Shifting of this force balance will affect the contact angle and thus the degree of wetting. In terms of energy, it can be said that this relation express the ratio between the energy gained and energy required to form a unit area interface between solid, liquid and gas. Figure 2.2 illustrates the force balance between the three phases involved in equation 2.4. If the surface tension of the solid-liquid interface is very high relative to the solid-gas interface, the droplet will reduce this interface area at the expense of increasing the liquid-gas interface area. If this is taken to the extreme, the solid-liquid interface will be equal to zero. The droplet will then assume the shape of a perfect sphere ($\theta_0 = 180°$), since this is the only way it can minimize Gibb's free energy (a sphere has the lowest surface/volume ratio theoretically possible). On the other hand, if the solid-liquid surface tension is very

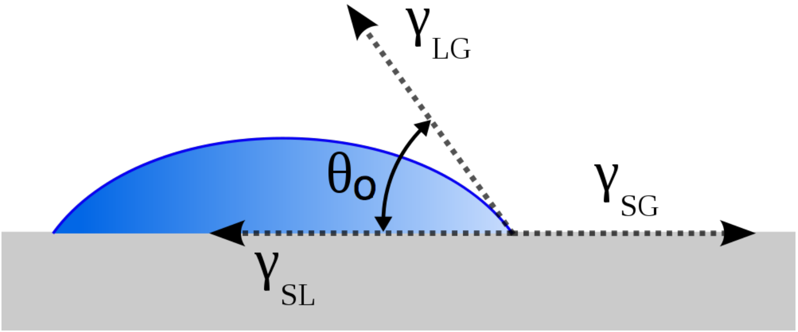

Figure 2.2: Illustration of the force balance involving surface tensions for a three-phase system in equilibrium when a droplet is placed on a flat solid substrate

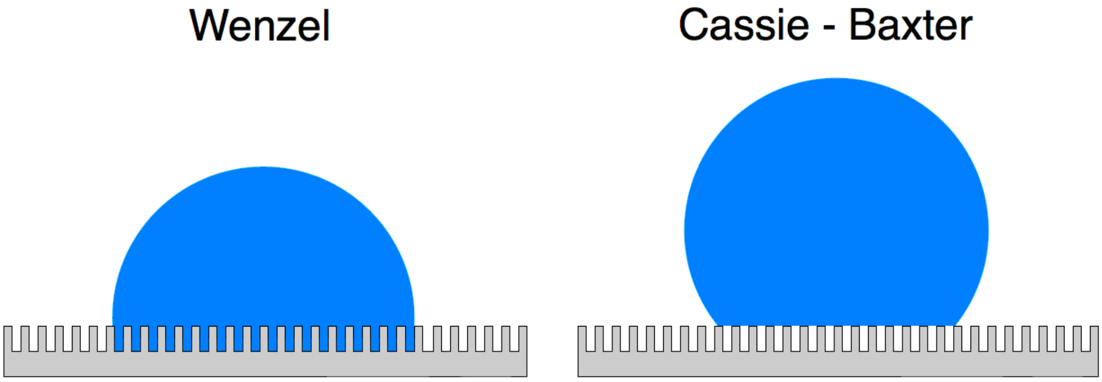

Figure 2.3: Schematics of the different wetting states on rough surfaces; homogeneous (Wenzel) and composite(Cassie-Baxter)

low relative to the solid-gas interface, the opposite will happen; the droplet will spread out as much as possible on the solid surface ($\theta_0 = 0°$).

2.1.3 Wetting on rough surfaces

Equation 2.4 expresses the contact angle on an atomic smooth surface. This is however an ideal case, as roughness affects the observed contact angle. Wenzel [35] proposed that the apparent contact angle θ is proportional to the real contact angle (θ, see equation 2.4),

$$\cos\theta = r\cos\theta_0 \tag{2.5}$$

by a roughness factor r, given as the ratio of the true area to the projected area perpendicular to a rough surface. This factor is always larger than unity. By insertion into Young's equation, one can see that the surface free energy of the solid-liquid interface is r times higher compared to a smooth surface. Thus, the effect of surface roughness is to augment the hydrophobicity.

Later, Cassie [36] proved that this model is only true for a homogeneous liquid/solid interface. When air pockets form at the interface, the surface must be considered as heterogeneous under a water droplet resting on a rough solid surface. The apparent angle θ of a rough surface surface that is composed of two fractions, with fractional area and contact angle f_1, θ_1 and f_2, θ_2 respectively is given by the Cassie-Baxter equation

$$\cos\theta = f_1\cos\theta_1 + f_2\cos\theta_2 \tag{2.6}$$

When f_1 ($f_1 = f_{SL}$, $\theta_1 = \theta_0$) corresponds to the solid-liquid fraction and f_2 ($f_2 = f_{LG}$ = 1 - f_{SL}, $\theta_2 = 180°$) corresponds to the liquid-gas fraction, then equation 2.6 reduces to

$$\cos\theta = -1 + (1 + r_f\cos\theta_0)f_{SL} \tag{2.7}$$

where r_f is the roughness factor of the wetted area. It is important to realize that when $f_{SL} = 1$, equation 2.7 reduces to the Wenzel model of a homogeneous surface.

2.2 Contact angle hysteresis

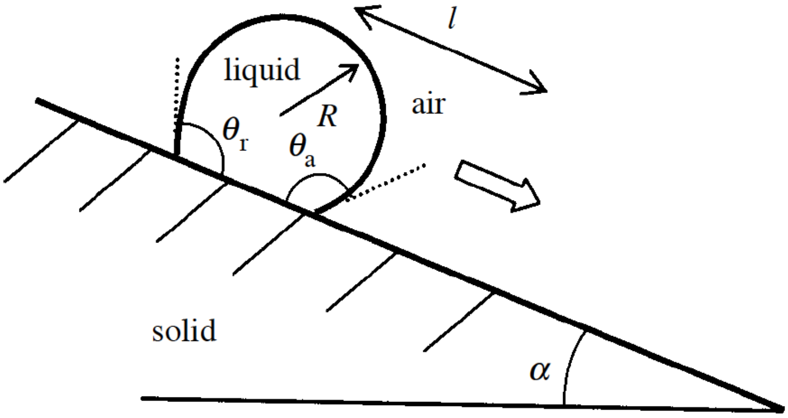

Figure 2.4: Schematics illustrating θ_{adv}, θ_{rec} and α for a rolling droplet [37].

The contact angle hysteresis (CAH) is defined as the difference between the advancing contact angle θ_{adv} and receding contact angle θ_{rec} of the triple line at a surface:

$$CAH = \theta_{adv} - \theta_{rec}, \tag{2.8}$$

which is illustrated in figure 2.4. This can be measured in two ways, by tilting the surface or add/remove volume to the water droplet by condensation/evaporation. When tilting the surface, the triple line of the droplet will be at a stationary position until it gains enough energy through gravity to overcome a potential barrier U as the tilting angle is increased. At this angle, called sliding angle α, the triple line will start moving down with a gravitational force. The contact angle is increased at the front side of the moving droplet and decreased at the rear side. This is because a gravity force-component $mg \cos \alpha$, acting parallel to the surface, shifts the force balance in equation 2.4. The difference between these angles are called the contact angle hysteresis.

Another method to measure the CAH is to add/remove volume to the droplet. When volume is removed through evaporation, the contact angle will decrease without changing the interfacial area until a certain contact angle is obtained. This is called the receding angle. Similarly, the advancing contact angle is the angle where the interfacial area starts to increase by adding volume through condensation.

2.3 Wetting properties

Surfaces are sorted into categories corresponding to their wetting abilities. A contact angle less than 90°(low contact angle) indicates that wetting of the surface is favourable in the terms of decreasing Gibb's free energy. By examining equation 2.4, this means that $\gamma_{SL} < \gamma_{SG}$. The fluid will spread over a large area and the surface is termed hydrophilic. When the angle is higher than 90°(high contact angle), wetting is unfavourable and the drop will minimize the contact area with the surface ($\gamma_{SL} > \gamma_{SG}$). The surface is then

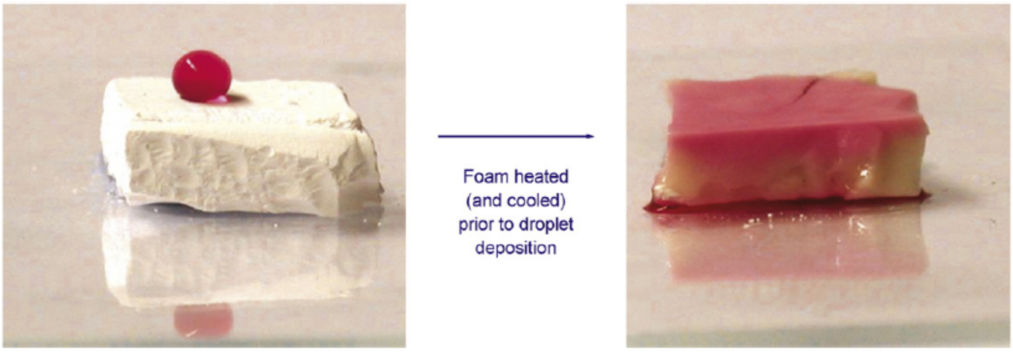

Figure 2.5: Illustration of the sharp transition between superhydrophobicity and superhydrophilicity of a porous material, induced by heating and made possible by the extreme surface roughness [39].

defined as hydrophobic. There are definitions of the extremities of these two categories; when the contact angles are less than 10°, the surface is termed superhydrophilic, while a superhydrophobic surface has a contact angle higher than 150° and CAH smaller than 10° [38].

When discussing superhydrophobic surfaces, it is often mentioned that the solid surface has a low surface energy. What is meant by this, is that the surface tension of the solid-gas interface is low, so that it is favourable in terms of minimizing the free energy to increase this interface area, and decrease the solid-liquid surface area (see section 2.1.2).

As was shown in section 2.1.3, the introduction of a roughness factor r_f change the apparent contact angle of the water droplet. By examining equation 2.5, it can be seen that introducing roughness to the surface ($r_f > 1$), the apparent contact angle θ increases when $\theta_0 > 90°$, while it decreases when $\theta_0 < 90°$. Thus, introducing surface roughness is a way to amplify the surface chemistry; a hydrophobic surface becomes more hydrophobic, while a hydrophilic surface becomes more hydrophilic. If the surface roughness is extreme, as is the case of nano-wires, the transition between superhydrophilic and superhydrophobic can be very sharp. Small changes in conditions, such as heating, has been demonstrated to induce small changes in the surface free energy, which induce switching between the two states [39].

In order for a surface to display superhydrophobic properties, it is necessary to have pockets of air trapped underneath the water droplets that are resting on the micro-scale asperities of the rough surface (Cassie-Baxter state) [40]. Transition from the Wenzel to the Cassie-Baxter state was observed by increasing the roughness factor r_f on a surface with micro-structured pillars [41]. The composite state is much less stable than the homogeneous state (Wenzel), so the droplet can easily fill the valleys between asperities with liquid [42].

The wetting properties of a surface is now well understood for a droplet at equilibrium, thanks to the models provided by Young, Wenzel and Cassie. However, models predicting the dynamic wetting behaviour of a droplet on a rough surface is not well understood, therefore most of the current theoretical research is currently focusing on this problem [43, 42, 44]. The contact angle hysteresis is a measure of the energy required to move a droplet across the surface when tilted. A droplet can have a high static contact angle and still be difficult to remove as it sticks to the surface (a phenomenon called pinning). Thus, some

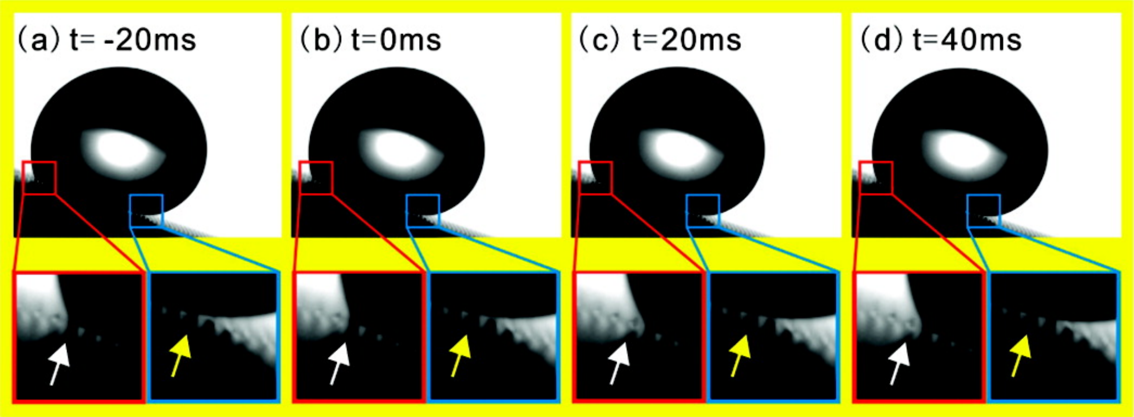

Figure 2.6: Continous recording of the dynamic wetting behaviour of a water droplet resting on micro-structured pillars. The arrows show the position of the advancing and receding triple points, which makes discontinous jumps across the micropillar surface [44].

researchers have the opinion that the static contact angle is irrelevant when examining the water repellency of a material, and that it is the dynamic wetting behaviour measured by the contact angle hysteresis, which is important [43]. It is believed that decreasing the CAH to give superhydrophobicity requires a transition from Wenzel to the Cassie-Baxter state [45].

2.4 Hierarchical surface roughness

Lotus leaves found in nature have two levels of surface roughness, with convex shaped cells on the micro-scale with superimposed nano-scale hydrophobic waxes (see section 1.8). The self-cleaning effect is dependent on this two-level roughness, due to the kinetics of droplet movement and the thermodynamics of wetting as explained by Gao et. al. [46]. They measured the advancing and receding contact angles of a smooth silicon surface and a surface with micro-fabricated pillars, both surface treated with dimethyldichlorosilane to achieve a low surface energy, to be $\theta_{adv}/\theta_{rec} = 104°/103°$ and $\theta_{adv}/\theta_{rec} = 176°/156°$ respectively. When a droplet moves across the pillar structures, it exhibits a phenomenon called contact line pinning, where the contact line moves in discontinuous "jumps" from one pillar to another. This is illustrated in figure 2.6. Because the droplet is in the non-wetting Cassie-Baxter state, it cannot wet the solid below the top of the pillars. This is the reason why pinning occurs.

In terms of kinetics, contact line pinning means that the droplets move between metastable energy states separated by energy barriers. The energy barriers is due to an attractive interaction between the water and the surface of the micro-pillars, termed disjoining pressure Π_D in surface chemistry [47]. Due to the disjoining pressure, the energy required to move the contact angle from a pillar to another at the advancing end is less than the energy demanded for removing the contact line from a pillar on the receding end. This is the reason why the receding contact angle is smaller than the advancing contact angle, and the reason for contact angle hysteresis. A way to decrease the contact angle hysteresis is obviously to increase the receding contact angle. This was done by depositing a cross-linked polymer network with nano-scale roughness on top of the pillars [46]. Due to the reduced contact area with the "nanorough" surface, the activation energy of contact angle recession was lowered.

2.5 Stability and transition of wetting modes

An important consequence of surface tension, which has not been discussed so far, is the pressure difference occurring across an interface. This is described by the Young-Laplace equation, given as

$$\Delta p = \gamma \left(\frac{1}{R_1} + \frac{1}{R_2} \right) \tag{2.9}$$

where R_1 and R_2 are the principal radii of curvature of the interface boundary[33]. If the interface is assumed to be spherical, as is the case of very high contact-angles, $R_1 = R_2$ and equation 2.9 reduce to

$$\Delta p = \frac{2\gamma}{r} \tag{2.10}$$

where r is the radius of the droplet. For a 1 mg droplet, whose diameter is 1.24 mm, $\Delta p = 235$ Pa, compared to the weight-induced pressure which is 12.2 Pa [48]. It can also be seen from this equation that smaller droplets exhibit larger pressure differences. It has been shown that pressing on a droplet can change the apparent contact angle [49]. Thus, the pressure difference across the interface will inflict the transition from Cassie-Baxter to Wenzel state. It may seem that the small pressure difference caused by the surface tension of a stationary droplet is insignificant. However, raindrops can reach high velocities and impact surfaces with pressures as high as $10^4 - 10^5$ Pa [50]. Also, the weight of a droplet may induce transition from the non-wetting to wetting state, even if gravity does not significantly change the droplet's shape [51]. Thus, the Cassie-Baxter state is only metastable for some structures and transition to a wetting state may occur by external stimuli, such as pressure and change of mass (condensation). The goal of designing a superhydrophobic surface is to make the Cassie-Baxter state more stable than the Wenzel state in terms of Gibb's free energy (see section 4.2).

Zheng et. al. [48] showed that droplets resting in the Cassie-Baxter mode on a micro-structured pillar surface, exhibited an inhomogeneous sinking inter-pillar water-air interface due to the hydraulic pressure. They found a critical pressure for which the non-wetting state breaks, given as

$$p_c = -\frac{\gamma f \cos\theta_0}{(1-f)\lambda} \tag{2.11}$$

$f = \frac{A}{A_c}$ and $\lambda = \frac{A}{L}$ are characteristic parameters of a periodic structure, given by the perimeter L, the cross-sectional area A and the apparent cell area A_c as seen from above (see figure 2.7). The top surface of the pillars is assumed to be planar for simplicity.

To achieve a high critical pressure, one could decrease the separation distance between the pillars, thereby increasing f. This however will lead to an unfavourable increase in the apparent contact angle, see equation 2.6. The cross-sectional shape of the pillar can

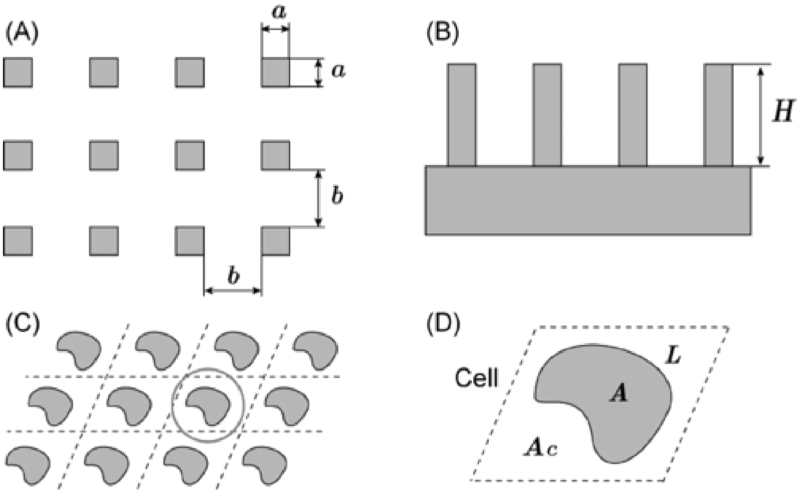

Figure 2.7: Illustration of a periodic micro-structural surface with the characteristic parameters given in equation 2.11 [48].

also be changed, so that the perimeter length L increases relatively to A. However, Zheng et. al. found that scaling down all the characteristic length scales to $\frac{1}{m}$ would increase the critical pressure m times. Hence, by decreasing a and b from 50 μm and 100 μm, to 50 nm and 100 nm respectively, it increases from $p_c = 296$ Pa to $p_c = 2.95 \cdot 10^5$ Pa.

Another important parameter for the transition between the two wetting states, is the height of the pillars H. If the inter-pillar perturbation depth of the liquid-air interface is larger than H, then the water will make contact at the base below the pillar cells. This will lead to a collapse of the non-wetting state. Zheng et. al. defined a geometric parameter called the slenderness ratio, defined as

$$\eta = \frac{HL}{A}. \tag{2.12}$$

A second parameter called the equi-energy slenderness ratio was defined in terms of the fractional area f and the smooth contact angle θ_0

$$\eta_e = -\frac{1-f}{f}\frac{1+\cos\theta_0}{\cos\theta_0}. \tag{2.13}$$

If $\eta > \eta_e$, then the Cassie-Baxter is stable (global energy minimum), while the Wenzel state is metastable (local energy minimum). This gives a critical height H_{cr} for pillars with constant shape and cross-sectional area. Thus, $H > H_{cr}$ is required for having a surface where the non-wetting state is stable. Whether this requirement needs be locally or globally for the droplet is not clear. However, Zheng et. al. suggested that some parts of the droplets could be in the non-wetted state, while other parts simultaneously collapsed into wetting of the surface [48].

From the discussion so far, it may seem that pillar structures on the surface should have as high slenderness as possible to maintain a stable Cassie-Baxter, thus ensuring superhydrophobicity. However, one has to take into account the effect of Euler buckling for pillars with a high value of η. Yu et. al. [52] deduced the critical water hydraulic pressure the pillars can accommodate before buckling, given as

$$p_c = \frac{\alpha f \pi^2 E}{4\eta^2} \tag{2.14}$$

where α is a proportional constant characteristic for the pillar geometry and E is the elastic modulus of the wax crystals. Through this analysis, it can be seen that the critical pressure decreases with increasing slenderness. Thus, it may seem that there is a trade-off between a stable non-wetting state and stability towards Euler buckling. However, in the same paper it was shown that the two-scale surface structure of papillose single cell with superimposed wax crystalloids of the lotus leaf can accommodate both properties, because the critical pressure were much higher than for single-scale wax pillars with the same slenderness ratio. Thus, it may seem that the multi-scale roughness is a strategy towards stabilizing the non-wetting state, even under high hydraulic pressures.

2.6 Measuring wetting behaviour

Following the discussion in this chapter, the wetting of a surface can be described quantitatively by the apparent contact angle θ, the sliding angle α, the advancing θ_{adv} and receding θ_{rec} contact angles. These quantitative parameters can be measured by using a contact angle goniometer, which basically consists of a CCD-camera measuring the shape of a droplet deposited on a stage, which can be tilted through a computer-controlled interface. Contact angles can be measured using a KSV Instruments CAM 200 contact-angle meter, situated in the Ugelstad Laboratory at the Department of Chemical Engineering at NTNU. The setup for this instrument is shown in figure 2.8.

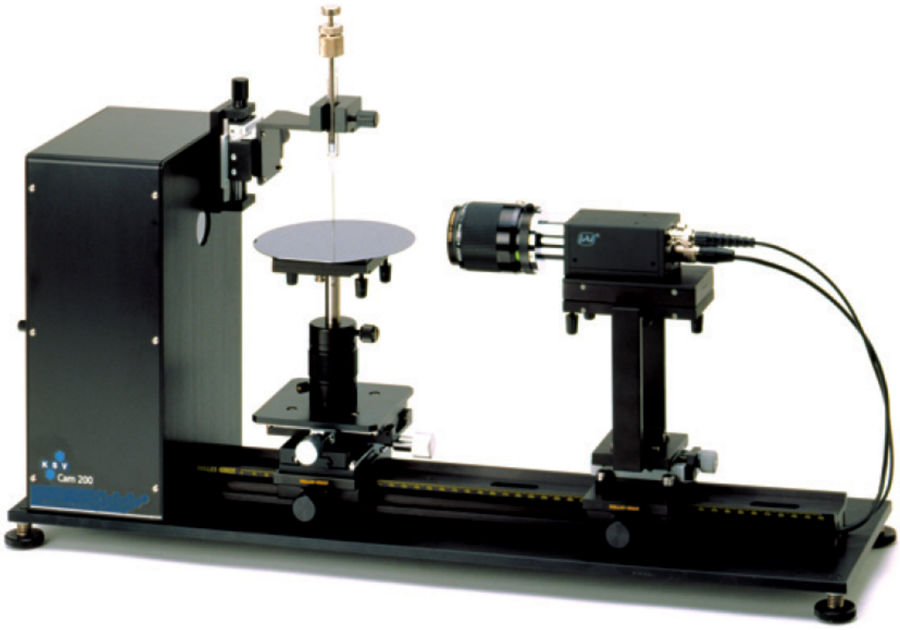

Figure 2.8: The experimental setup of a KSV CAM 200 contact-angle goniometer used to measure the equilibrium and dynamic wetting behaviour of a droplet on a surface [53].

Chapter 3

Fabrication of superhydrophobic surfaces

Fabrication of superhydrophobic surfaces with a contact angle $> 150°$ and a contact angle hysteresis $< 10°$, is usually done by introducing surface roughness and change the surface chemistry in order to achieve a lower surface energy. As was explained in section 2.1.3, increasing the surface roughness increases the apparent contact angle of a hydrophobic surface. In addition, reducing the surface energy of the solid-water interface, reduces the adhesive forces and the energy required to initiate the rolling motion of a water droplet.

Methods of fabricating superhydrophobic surfaces can be divided into two categories based on the approach, namely top-down and bottom-up methods. Top-down approaches involve sculpturing of a bulk material with traditional micro-fabrication techniques such as cutting, milling, patterning and etching, where material is removed selectively to achieve nano-scale geometries. In contrast, bottom-up methods use single molecules as building blocks to self-assemble or self-organize larger structural assemblies.

Both of these approaches have advantages and disadvantages that depends upon the application. Top-down methods usually gives the researcher better control of the manufacturing processes and the final result is easier to predict. It is however generally more time-consuming and expensive compared to bottom-up methods, which makes mass-production of large atomically precise structures possible. On the other hand, bottom-up methods typically involves a higher degree of complexity and is more difficult to control. Therefore, each fabrication method is often application-specific.

Also, researchers have used either the intrinsic hydrophobicity (low surface energy) of the material used in fabrication, or coated the final structure with a thin hydrophobic layer. The first approach is advantageous as this simplifies the fabrication process. In addition, thin coatings tend to degrade over time due to chemical and mechanical wear. However, the surface energy of useful construction materials may not always be low enough to allow superhydrophobicity. Different methods within each category will be discussed and some examples of engineered superhydrophobic structures will be shown.

3.1 Top-down

3.1.1 Photolithography

Photolithography is a conventional process within micro-fabrication, which has been used in the semiconductor industry for several years to transfer patterns on the surface of a wafer. The process procedure typically contains eight different steps [54]. First, the substrate is cleaned of contaminants and dehydrated to improve adhesion. Then, a layer of a liquid

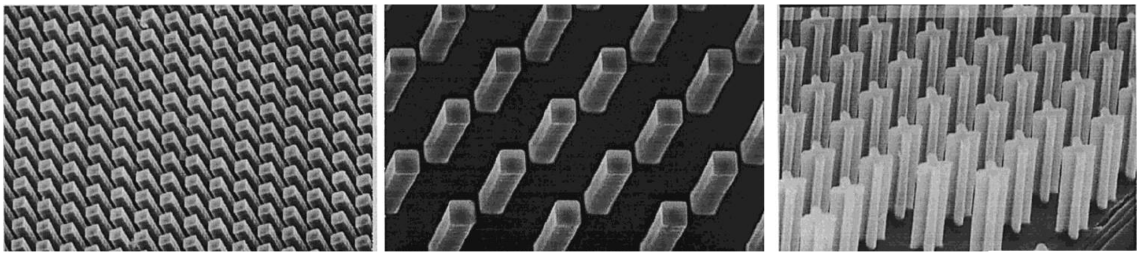

Figure 3.1: Well-defined surface structures can be produced by photolithography and subsequent etching in the silicon substrate [43]

photo-active polymer is applied on the substrate surface through spin-coating, where the thickness of the resist layer is controlled by the rotation speed. To further enhance adhesion between the resist and the substrate, the wafer is soft baked on a hot plate. The wafer is placed under a mask-aligner to control where on the wafer the pattern should be applied, followed by exposure. Photolithography can be divided into categories depending on the radiation source used; UV, electron-beam or X-ray. UV-lithography is the most used as this method is often most convenient, although e-beam and X-ray lithography are able to produce controlled structures with finer resolution. The exposure step makes the resist hard and insoluble (negative) or soft and soluble (positive) depending on what type of resist is used. The exposure step is very important as this is the step where the wafer is actually patterned. Following exposure, the resist is often baked once more on a hot plate (post-exposure bake), before a developer chemical is applied to dissolve the soluble parts of the resist. After this step is performed correctly, a resulting three-dimensional structure will be visible on the wafer. For best stabilization of the resist structure, a final baking step is performed at the end (hard bake). The wafer is then ready to be characterized by optical microscopy, SEM or AFM for the finest structures. If the pattern is not satisfactory, the resist can be removed by acetone and the process restarted to step 1. Depending on the application, the resist pattern is used as a mask for selective etching or ion implantation of the substrate material.

The advantage of photolithography is that it is a technique which enables the researcher to create well-defined three dimensional structures on the sub-micron scale. For this reason, it has mostly been used to create surfaces for examining the superhydrophobic phenomenon and to establish new theoretical models of wetting. One of the earliest works by Öner et. al. to examine the wetting quantitatively on a micro-textured surface, was done using photolithography to produce three dimensional posts by etching on a silicon wafer with various size, shapes and separations [43]. As was discussed in section 2.6, the wetting properties (θ, θ_{adv}, θ_{rec} and α) can be quantized by a contact angle-goniometer for different surfaces, which can be used to deduce theory based on the geometry parameters of the surface structures. Öner et. al. found that a separation distance between the posts lower than 32 μm resulted in a non-wetting state (Cassie-Baxter) where the wetting was independent on the height of the posts. By increasing the separation distance between the posts by more than 32 μm resulted in a rapid decrease in both θ_{adv} and θ_{rec}, a sign that the droplet transformed into a wetted state (Wenzel).

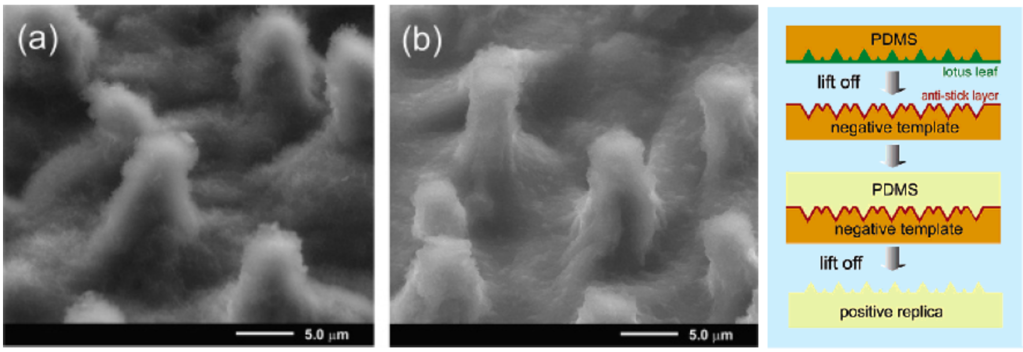

Figure 3.2: (a) The lotus leaf surface structure and (b) the replicate in PDMS have very similar surface morphology. (c) The replication process steps using PDMS [55].

3.1.2 Replication

Replication is a method that involves creating a template for which an inverted replica can be produced from. Although it is a top-down method, the process steps are rather inexpensive and fast compared to conventional photolithography for producing nano-structures. The quality of the replicate is depending on the spatial resolution of the template, so if reliable templates with details at the nano-scale can be fabricated, this method has a potential in mass-production of nano-structured materials.

Replicates of the surface structure of the lotus leaf has been achieved by Sun et. al. [55]. In this work, they casted liquid polydimethylsiloxane (PDMS) over the leaf's surface and let the solution cure at room temperature to form the template. PDMS is a soft polymeric material with intrinsic hydrophobicity (contact angle about 105°). After solidification of the PDMS template, the surface was coated with a monolayer of anti-sticking layer (trimethylchlorosilane (TMCS)). Then, liquid PDMS was poured over the template to fill all the voids and valleys. After curing, the resulting PDMS replicate displayed a very accurate copy of the micro- and nano-scale surface of the lotus leaf 3.2, and the contact angle was measured to be 160°.

3.1.2.1 Nanoimprint lithography (NIL)

Nanoimprint lithography (NIL) is a technique which can be categorized under replication. It was first demonstrated in 1995, when it was used to create an array of holes with diameters of about 25 nm and depth of about 100 nm in a thin film of polymer resist [56]. Later, the technique has shown to be able to fabricate structures with a resolution down to 5 nm [57]. It uses a mechanically rigid stamp, often produced by electron-beam lithography, that is pressed down into a thin film of a soft polymer, which are able to conform to the surface roughness. Before the stamp is removed, the film is hardened. The resolution of the final imprint pattern is limited by the master stamp resolution and the process conditions. The advantage of NIL compared to other nanolithographic techniques, is that once the stamp is fabricated, it can be used up to tens of thousands of times without significant wear [58]. Thus, it may seem that it is one of the most promising top-down methods for industrial mass-production of nanostructured materials.

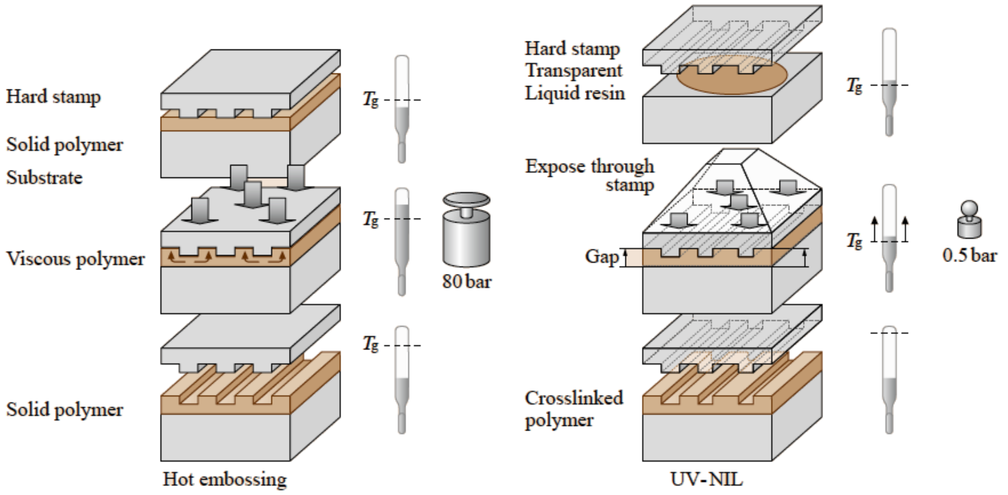

Figure 3.3: The TNIL process, often called hot embossing, use heating and cooling to soften and harden the polymer film, while UV-NIL uses liquid resist at room temperature and UV light for curing [58].

Several variations of NIL exists. When using thermal nanoimprint lithography (TNIL), the substrate that the thin film is resting on is heated, thus increasing the viscosity of the polymer so that it can flow more easily when the stamp is squeezed down. Hardening is done by cooling the substrate while the pressure is maintained, before finally removing the stamp. Often, the stamp has to be coated with an anti-adhesive layer to ease the removal of the stamp without destroying the polymer surface relief. An alternative to TNIL is UV nanoimprint lithography (UV-NIL), which uses a resist that is liquid at room temperature, so that no heating is required. Curing is done by exposing the resist to UV light through a transparent stamp. UV-NIL allows the use lower pressures, since the resist is already liquid at room temperature. Thus, also stamps made of softer materials can be used. The process steps are summarized in figure 3.3. The imprint process can be done in a parallel process on large-area substrates or in small, fast repeated stepping process. After the imprint, the nano-structured polymer film can be used by itself, or as a mask for further processing of the underlying substrate.

Important process parameters for the imprinting is the pressure that is applied to the backside of the stamp, and the viscosity of the polymer, which is determined by material properties and the temperature used for softening. The applied pressure needs to be high enough to ensure complete transfer of the stamp surface relief. In addition, using high pressures can be used even out surface roughness of the underlying substrate. However, a too high pressure will destroy the stamp. Lower pressures can be used if the viscosity of the polymer is lowered. The viscosity of polymers are determined by the molecular weight, M_w of the polymer chains. The viscosity of the polymer decreases with decreasing M_w, which means that imprinting using a low M_w polymer can be achieved at lower temperatures. Imprinting at low temperatures are also feasible in the way that less time is required for heating and cooling, thus increasing process efficiency.

NIL has so far been a promising candidate to replace more traditional nano-lithography

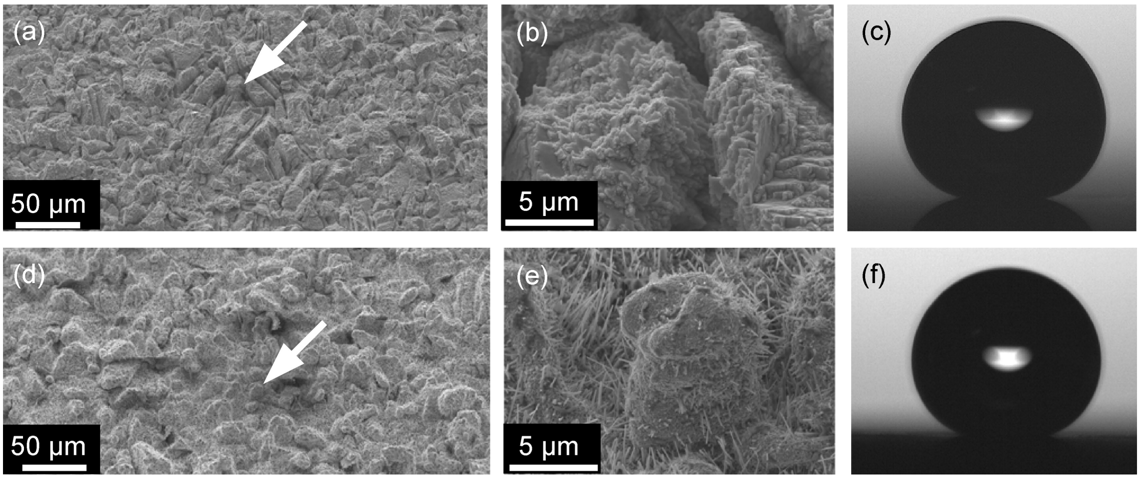

Figure 3.4: (a-c) SEM micrographs of etched polycrystalline copper surfaces and a measured contact angle of 171°. (d-f) CuO nano-wires grown on the micro-rough copper surface, giving a contact angle of 169° [59].

techniques for large-scale production. This advantage can be used in the production of superhydrophobic surfaces with both nano- and micro-scale roughness. Even though surface-effects occur on the nano-scale, wetting is also a macroscopic effect due to the droplet size, thus relatively large areas have to be covered to be of any practical use. Thus, using NIL as a parallel or in a serial step-and-scan process to produce arrays of posts, can extend the experimental verification of superhydrophobic theory down to the nano-scale. Also, NIL could be combined with traditional photolithography to produce multi-scale roughness. Thus, NIL may be a useful experimental tool to produce surfaces that can be tested against the wetting models described in the last section.

3.2 Bottom-up

3.2.1 Crystal growth

Crystallization methods can be used to grow structural features and introduce micro- and nano-scale roughness, leading to superhydrophobicity of an intrinsic hydrophobic material or coating of an additional hydrophobic layer. Crystallization of polycrystalline copper plates was done by the Group of Bionanotechnology at NTNU, lead by Associate Professor Pawel Sikorski [59]. In this work, both top down and bottom up methods were used. First, macro- and micro-roughness were produced by using a transparent with toner ink printed by a regular laser printer as a mask, followed by etching using $CuCl_2$ and HCl. Nano-roughness was introduced by growing CuO nano-wires on the surface by thermal oxidation in air at 500°. Finally, the nano-rods were coated with fluorocarbons to reduce the surface tension. The resulting micro-texture is shown in figure 3.4.

Roughness at the nano-scale has also been achieved by growing carbon nanotube (CNT)s on stainless steel substrates using chemical vapor deposition (CVD) [60, 61, 62, 63]. CVD is a general fabrication method used in the semiconductor industry to deposit thin films of various materials, where a substrate is exposed to a reactive precursor gas. The different forms of CVD is defined by their process conditions, i. e. pressure ranges, and activation processes, for instance plasma-enhanced chemical vapor deposition (PECVD) which utilize plasma generated in an electric field to enhance the chemical reaction of the precursor gas. To grow CNTs, it is usually necessary to deposit a metal catalyst on the substrate prior to growth, such as nickel, cobalt, iron or a combination [64]. The substrate is then heated to typically 700°, and a process gas (ammonia (NH_3), hydrogen (H_2), argon (Ar) or nitrogen (N_2)) together with a carbon-precursor gas (acetylene (C_2H_2), ethanol (C_2H_5OH), methane (CH_4) or ethylene (C_2H_4)) is fed into the reaction chamber. The carbon gas reacts at the interface of the substrate and the catalyst particles to form CNTs. As the CNTs grow outwards from the surface, the catalyst particle stays at the end until it is separated too far from the surface for the reaction to continue.

Production of multi-walled CNTs on the surface of stainless steel has been achieved without any pre-deposition of catalyst, using the iron-based material surface of a commercial-grade SS 304, itself acting as the catalyst [62]. Uniform layers of CNTs with diameters ranging from 20-70 nm was produced on plate, powder and grid surfaces by this method (see figure 3.5). Highly aligned CNTs can be grown using PECVD, where the CNTs grow in the direction of the applied electric field in the reaction chamber [60]. It is however thought that the directionality does not play any role in the wetting properties of surface itself, as the micro- and nano-texture on the surface of the lotus leaf are irregular and random [30]. Fabrication of superhydrophobic stainless steel surfaces can be exploited for several applications, see section 4.3 and 4.5.

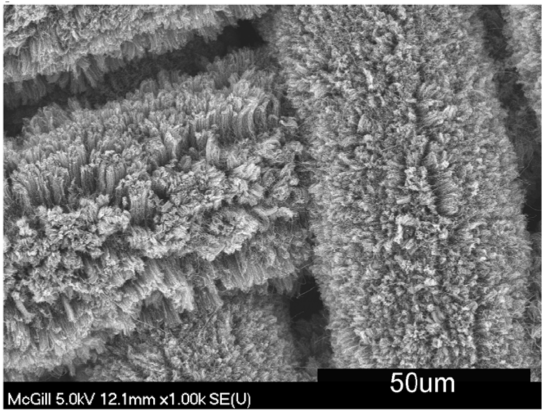

Figure 3.5: CNTs grown on the surface of a stainless steel grid [62]

3.2.2 Phase separation

Phase-separation of a multi-component mixture induced by changes in temperature or pressure can be used to create a three-dimensional superhydrophobic surface [38]. In the sol-gel process for instance, one starts with a chemical solution (sol) that separates into two phases by environmental change, where one of the phases forms a solid continuous network of discrete particles or polymers (gel). The second phase, which is often a liquid, can then be removed to create a solid porous structure. This occurs through a drying process, which typically leads to shrinkage and densification of the solid phase. The size of the pores can be controlled by controlling the rate of phase separation relative to the rate of solidification. If the drying process is not done in a controlled manner, it can lead to cracking and collapse of the structure. Often, thermal treatment (firing) is necessary to enhance the mechanical stability .

Phase-separation is an interesting method to fabricate superhydrophobic structures because they involve low costs and easy fabrication steps, where most process steps can be done close at room-temperature. Another reason why these porous structures are interesting is because they can be cut and abraded without loosing their random surface roughness. These types of materials have been used for many years in filtration, catalysis and in chromatographic analysis. In the work done by Shirtcliffe et. al. [65], it was shown that it is possible to make intrinsically superhydrophobic organosilica foams through the sol-gel process. There was no need for further surface treatment after phase separation, as the network of interconnected organosilica particles were hydrophobic itself because of its chemical nature. Because the foam is intrinsically hydrophobic, the non-wetting properties of the surface would not diminish with abrasion as it would be for surface coated rough materials.

3.2.3 Assembly of colloidal particles

Another bottom-up strategy is to assemble colloidal particles closely packed on a surface through attractive van der Waals forces between the spheres in an ordered or non-ordered structure. Ordered structures of mono-disperse particles (particles with narrow size distribution) can have other applications, such as acting as a photonic crystal, which are useful in optical applications. The magnitude of surface roughness can be tuned by choosing the particle size. Materials like silica [66] and polymer spheres [67] can be used and functionalized with chemical side-groups to enhance hydrophobicity. This method is also inexpensive, it can be applied to large surface and does not require any special equipment.

3.3 Hierarchical surfaces

The lotus leaf's surface has a hierarchical roughness at the micro- and nano-scale as discussed in section 1.8. It has been shown that this two-level hierarchy enhances the hydrophobicity, see section 2.4. Also, hierarchical surfaces have a higher resistance against mechanical wear compared to a surface with only nano-scale roughness, as a smaller fraction of the surface area is available for wear damage [68]. Theoretical studies have shown that hierarchical surfaces lowers the energy barrier associated with moving a droplet across a surface and prevention of conversion from a Cassie-Baxter state to the Wenzel state [40]. Thus, the trend of research in recent years has been towards producing surfaces with multiple-scale roughness [38]. Some examples have been discussed already, like replication of the lotus leaf using a soft polymer and crystallization of CuO nano-wires and CNTs on micro-textured surfaces. Another way to achieve hierarchical surface roughness is through combining the different methods discussed in this chapter. For instance, CNTs have been grown on the surface of an array of colloidal particles [69]. Also, well-defined posts at the micro-scale in silicon can be produced by photolithography, followed by spraying on a layer of CNTs [70]. In this work, it was shown that water droplets have a higher degree of non-wetting for the hierarchical surface, compared with having only CNTs on a flat substrate. Also, through tribological studies using AFM, CNTs were shown to have a higher mechanical durability than the lotus wax [70].

Chapter 4

Applications of superhydrophobic surfaces

The examples presented in chapter 1 have served as a source of inspiration for various applications. As engineers, we have a much larger toolbox available when it comes to material selection and fabrication process, than any given biological system have. However, the biological systems are dynamic in the sense that they respond rapidly to changes in the environment, and have the ability to self-repair minor damages [71]. Also, they have an extraordinary ability to produce well-controlled structures down to the nano-scale. This is something that is difficult for an engineer to mimic. Nature's design is seldom optimized from an engineer's point of view. Therefore, one cannot simply copy nature blindly. A successful design must be application-specific. Superhydrophobic surfaces inspired by the legs of a water strider, the water fern, the back of the Namib Desert Beetle or the surface of the lotus leaf discussed in section 1, have a wide range of possible applications. Among them are self-cleaning, anti-fouling, anti-corrosion, hydrate inhibition, anti-icing, water-harvesting and drag reduction, which will be discussed in more detail in this section.

4.1 Self-cleaning

One of the first applications of superhydrophobic surfaces mimicking nature was within self-cleaning. Sto Corp. (USA) commercialized an acrylic-based exterior paint in 1999 under the registered trademark Lotusan®, named after the self-cleaning effect of the lotus leaf described in section 1.8 [72] (see figure 4.1). According to the company, the paint protects against particle contamination, fungal and algae growth, excellent weather resistance and high water vapour permeability due to the micro-texture similar to that of the Lotus leaf.

Figure 4.1: The Lotusan®paint from Sto Corp. have self-cleaning properties [72].

Self-cleaning surfaces can be used to reduce maintenance costs of exterior buildings, as they do not need to be cleaned regularly with surfactants. However, as the surface is exposed to the outside environment, the coating may be degraded by various ways of chemical and mechanical abrasion, such as pollution and wind. Because maintaining micro- and nano-scale roughness is essential for the self-cleaning, such kind of surfaces are very vulnerable to environmental conditions. If the coating is quickly degraded by these mechanisms, it has to be re-applied regularly, which counteracts the purpose of making the surface permanently self-cleaning. As discussed in section 3.2.2, a porous layer can retain the micro-roughness even if the outermost surface is abraded. Thus, this may seem as an appropriate approach of making self-cleaning surfaces that are exposed to harsh environmental conditions.

Other applications where self-cleaning can be advantageous besides exterior paint, may be solar panels or windows. If solar panels are covered with particles and dust from pollution, the intensity of the solar radiation being absorbed would be reduced. If a self-cleaning coating is applied, water from raindrops would be sufficient to clean the surfaces, similarly with windows. A self-cleaning coating for these kind of applications need however to be optically transparent. If the scale of roughness on the surface is increased, the scattering of light incident on the surface is also increased, which reduces the transparency [38]. Thus, to avoid diffraction of visible light, which have a range of wavelengths from $380 - 800$ nm, the surface features have to be less than about 100 nm. Because of this, arrays of nanorods fabricated by crystal growth seems a feasible way to go, as they are highly resistant to pressure, have extremely high specific surface areas and can be optically transparent to their tiny dimensions [38]. A self-cleaning, anti-reflective coating inspired by both the lotus leaf and the nipple structure of the moth eye was produced by growing ZnO nanorods using CVD [73]. The resulting surface coating had a hierarchical surface roughness with a hight water contact angle ($>160°$), a low CAH ($2°$) and a low average reflectance in the visible range (2.5%).

4.2 Anti-icing

Icing can lead to minor problems like icing on the front wind-shield of your car, or more serious consequences like bursting pipelines due to hydrate formation (see section 4.3), making roads slippery or cause loss of lift force on aircraft wings. Traditional methods of removing ice are mechanical scraping or through melting by heating or applying anti-freezing chemicals like salt or glycerol. However, these methods are not sustainable as they are either expensive, can cause abrasive damage to the surface (leading to other problems such as corrosion) or they are toxic to the environment. Superhydrophobic coatings can have permanent anti-icing properties if the material has enough mechanical stability and resistance towards degradation. The mechanism of ice formation has been examined on hydrophilic, hydrophobic and superhydrophobic surfaces [74]. In this work, they examined the dynamics of droplets hitting supercooled surfaces at a tilt of 30° using a high-speed camera. Three kinds of surfaces were made; smooth aluminium (hydrophilic), smooth fluorinated silicon (hydrophobic) and micro-fabricated fluorinated silicon (superhydrophobic). It was seen that while ice formation occurred for the first two surfaces, the superhydrophobic surface remained free of ice after 10 minutes with temperatures down to -25°, because the impacting droplets simply bounced off the surface, minimizing the heat transfer at

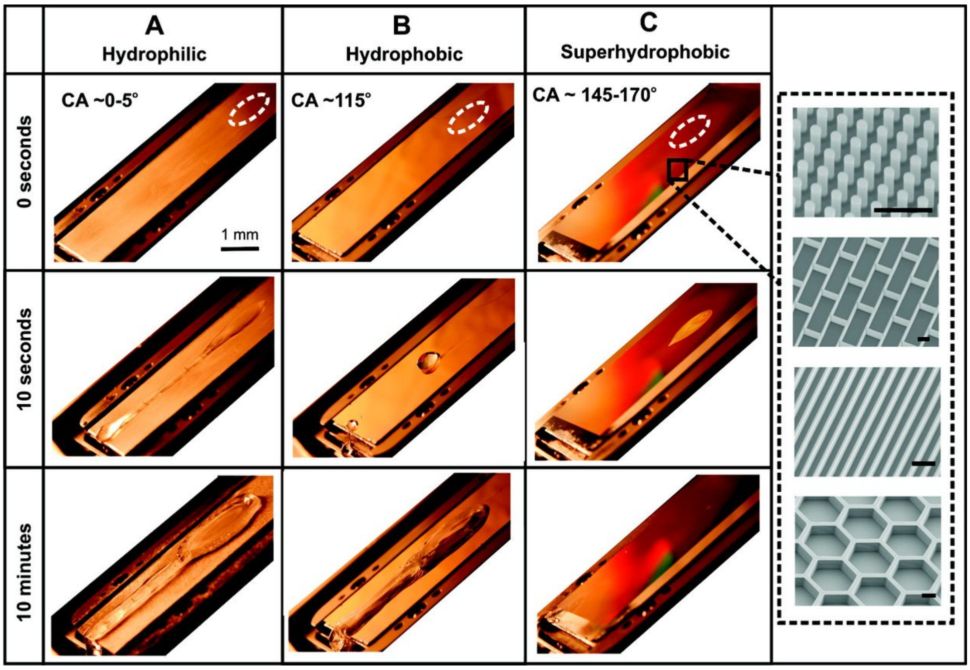

Figure 4.2: Figure showing accumulation of ice over 10 minutes for a hydrophilic (A) and hydrophobic (B) surface, but not for superhydrophobic (C). Three kind of superhydrophobic micro-structures are inset (arrays of posts, bricks, grating and honeycomb) [74].

the liquid-solid interface. At -30°, even the superhydrophobic surface became coated by ice. However, it was shown that the ice remained in the non-wetting Cassie-Baxter state (section 2.1.3), so removal of ice is still easier than for the other surfaces.

Another important discovery in this work was the effect of different types of microstructure made by photolithography and etching in silicon (posts, ridges and closed cell-shaped like bricks and honeycombs). The surface with an array of posts exhibited the highest static contact angle (170°). However, another important parameter for ice-repellent, or iceophobic, surfaces is the dynamic pressure stability, i. e. the maximum liquid pressure the system can tolerate before the non-wetting state breaks down [74]. This is important for applications where water droplets hit the surface at very high velocities (in automobiles or aircraft wings). With this in mind, the brick-wall structure ($\theta = 158°$) exhibited superhydrophobic properties at pressures up to 60 atm, while the Cassie-Baxter state was not maintained for droplets impacting the post array surface at 10 cm in ambient conditions. Thus, the surface structure has to be designed according to the specific application it is intended for.

4.3 Hydrate inhibition

During natural gas production, formation of methane hydrates is an unwanted process as it tends to block pipelines. Methane hydrate is a solid clathrate hydrate, which consists of methane gas molecules trapped in cage-like structures of crystalline hydrogen-bonded water molecules, similar to ice [75]. As methane gas is pumped up from deep-water reservoirs at high pressures, water condense at the pipeline side-walls due to the low temperatures involved. Other hydrate compounds can also be formed from larger hydrocarbon molecules such as ethane and propane.

The oil industry spends a large amount of resources dealing with hydrate formation each year. Common methods used are to reduce the pressure, increase the temperature or dissolve the hydrates by chemicals introduced into the pipelines. Removal of hydrates must be carefully controlled, as the hydrates dissociates into gas and water. If this process is performed too fast, it will lead to rapid gas expansion. This can cause ejection of fluid from the wells and blow-outs [76].

Due to the potential problems associated with hydrate formation and the fact that none of the conventional methods are sustainable, make the use of a superhydrophobic coating a promising strategy. Such kind of coatings would prevent condensed water to stick to the surface and potentially prevent hydrate formation. As mentioned in section 3.2.1, carbon nanotubes can be grown directly on steel alloys using CVD. The carbon nanotubes provide the nano-scale roughness on the surface, as well as mechanical strength, which increase the duration of the superhydrophobic coating [70].

4.4 Drag reduction

As discussed in section 1.3, the ridge-like structure on the surface of the shark skin reduce the drag under water by restricting the formation of turbulent vortices above the surface. Therefore, the area which high-velocity vortices interact with the skin surface is significantly reduced, leading to a drag reduction of about 9.9% [10]. In addition, the water fern discussed in section 1.7 have the ability to retain a thin layer of air at the leaf's surface. The effect is similar to that of the shark skin: to reduce fluid drag along the surface.

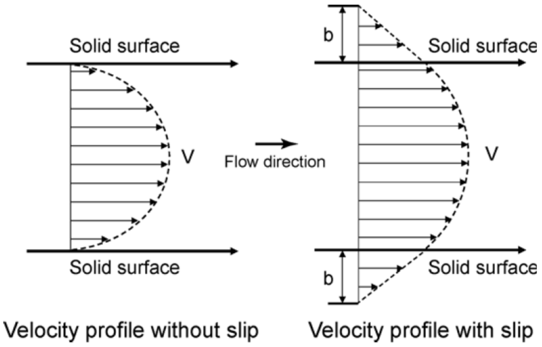

Figure 4.3: The figure illustrates the velocity profile for laminar flow in a channel, showing the difference between the no-slip and slip condition [77].

This could have a potential in developing biomimetic coatings for reducing drag experienced by large ships. From 1950 to 2001, the total fuel consumption in the marine industry worldwide increased by a four-fold [78]. The exhaust gases and particles released have serious impact on the marine life and must be reduced to a minimal amount. In addition, reducing the fuel consumption are of great economical interest. Similarly, reducing the air drag experienced by aeroplanes would be beneficial due to the same reasons. In addition, drag reduction is of interest in micro/nanofluidics based biosensor applications [79]. As the length scale of channels decrease by a two-fold, the resistance associated with liquid flowing through is increased by a four-fold [80]. Thus, reducing the fluid drag would have a great impact in this field.

Drag reduction could be achieved by mimicking the mechanics behind the drag reduction in shark skin and air-retention in water ferns. It has already been exploited in the case of making riblets similar to those seen on the shark skin [11] for decades. By covering about 70 % of the surface of an aircraft, a drag reduction of 3 % was achieved [10]. Other tests were done by designing riblet structures on the surface of ships, pipelines [10] and more recently competitive swimsuits fabricated by Speedo [81]. However, all designs have so far yielded a maximum drag reduction of only 10 %.

Superhydrophobic surfaces as those shown in the example of the water fern (see section 1.7) seems a better strategy for drag-reduction. Generally, it is assumed that the flow velocity is equal to zero at a solid-liquid interface (no-slip condition), and that it increases continuously with moving distances normally outward from the surface [82]. However, this assumption has been disputed for hydrophobic surfaces, which exhibits slip [83]. The degree of slip exhibited by a surface is defined as slip length b, the vertical length by which the velocity distribution is displaced compared to the velocity profile with a non-slip condition (see figure 4.3). Superhydrophobic structures, like the water fern has been shown to have a large slip length, leading to a drag reduction of up to 50%, compared to only about 10% for shark skin replicas [77]. This effect, called "giant liquid slip", is thought to be due to the air film retained at the surface [28]. Thus, superhydrophobic surfaces, which are able to retain air when submerged under water for prolonged time, may seem to be the best drag-reduction strategy.

4.5 Anti-corrosion

So far, some of the phenomenons of superhydrophobic surfaces like water-resistance and air-retention have been discussed. Fabrication of superhydrophobic surfaces on metal were also discussed in chapter 3. It is feasible to adopt the strategies discussed so far to fabricate metal coatings for anti-corrosion purposes. Previous work have developed a superhydrophobic film on a copper metal surface [84]. The surface were found to have a contact angle of 158°. It was also tested for anti-corrosion properties, and after immersion in seawater for a month, no change in the contact angle were detected. It is believed that the anti-corrosive property is because of the retention of air at surface, so that the surface is practically kept dry even when submerged under water.

4.6 Water harvesting

Finally, wetting behaviour can be utilized for collection of water in hot and arid areas. As discussed in section 1.6, the Namib Desert Beetle already accomplishes this due to the alternating hydrophobic and hydrophilic regions. A biomimetic device inspired by this design was developed by Zhai et. al. [85]. In this work, hydrophilic regions were patterned on a superhydrophobic surface by dispensing droplets of a 1% FITC-PAH polyelectrolyte solution using a micro-pipette, in an array of spots with diameters of 750 μm. The superhydrophobic background had $\theta_{adv}/\theta_{rec} = 172°/169°$, while the hydrophilic spots had $\theta_{adv}/\theta_{rec} = 144°/12°$. Thus, water droplets condensing on the surface rolled off the superhydrophobic areas and eventually stuck to the hydrophilic regions, where they were highly pinned.

Chapter 5

Future work

From the presented topic, it is clear that there are many challenges and unanswered questions left, both connected to understanding the mechanics and the fabrication process of durable and robust superhydrophobic nano-structured surfaces suitable for the commercial market. From a personal view, it would be most interesting to further investigate the connection between nano-structures and hierarchical roughness, and the mechanics of wetting. As mentioned earlier, the Group of Bionanotechnology at NTNU have experience with making superhydrophobic surfaces from thermal oxidation of copper films, as was disscussed in section 3.2.1. The method is fairly simple, once the optimum process parameters has been found. One could extend this work further by patterning the surface by photolithography to make defined superhydrophobic regions or dual-scale roughness. Furthermore, it would be interesting to try to replicate the structures in PDMS and compare the wetting behaviour, as this seems a suitable method for large-volume production. Growth of CNTs on steel surfaces that enables superhydrophobicity was also discussed at group meetings in the project group. However, due to a lack of previous experience and complexity of this process, it may be more suitable as a PhD-project. In a longer time-perspective it would be interesting to study the nano-mechanics of wetting experimentally by producing sub-micron pillars, either by photolithography, nanoimprint lithography or a combination. However, this task may also be more suitable for a PhD project like the CNTs, due to the complexity and the associated costs.

Chapter 6

Conclusion

The field of biomimetics is an approach towards solving engineering challenges, by using the various designs in nature as a source of inspiration. Through millions of years with evolution, biological systems have been optimized to adapt to the various conditions on this planet. Some of these processes have resulted in functional materials, such as robust materials by structural arrangement of weak minerals and proteins, anti-reflective coatings, water harvesting through condensation, friction reduction under water or through sand, reversible adhesion to virtually all kinds of surfaces, water floating or self-cleaning and anti-adhesive surfaces. With the recent advances in methods for characterization, manipulation and simulation at length scales down to the atomic level, the underlying mechanics can be studied to a much greater level of details than before.

Further investigations presented in this report was devoted to the phenomenon of superhydrophobicity, or surfaces with extreme water-repellency. To maintain superhydrophobic surfaces, it was shown that designing a hierarchical surface structure with roughness both at the micro- and nano-scale is crucial to ensure a stable non-wetting Cassie-Baxter state. It was discussed that it is important to study both the equilibrium and the dynamics of wetting of surfaces. Terms like surface tension, surface energy, contact angle, hysteresis, and pressure stability was defined. External factors facilitating transitions between non-wetting and wetting states were also discussed.

Different fabrication methods for producing the required multi-scale surface roughness was reviewed. Both top-down and bottom-up approaches are feasible, with certain advantages and disadvantages. While top-down methods such as photolithography gives the user a very good control over the final result, bottom-up methods can be more difficult to predict due to their higher complexity. Top-down methods are therefore mostly used for studying the mechanics of superhydrophobicity, while bottom-up methods may have a larger potential for industrial applications due to lower cost. Furthermore, several examples of potential applications where superhydrophobic surfaces may play a crucial role were discussed, such as self-cleaning, anti-icing, protection against corrosion, formation of hydrates and facilitation of drag reduction. Depending on the desired application, different aspects must be taken into account when designing the surface.

Bibliography

[1] S. Nikolov, M. Petrov, L. Lymperakis, M. Friak, C. Sachs, H. O. Fabritius, D. Raabe, and J. Neugebauer, “Revealing the design principles of high-performance biological composites using ab initio and multiscale simulations: The example of lobster cuticle,” *Advanced Materials*, vol. 22, no. 4, pp. 1–8, 2010. (Cited on page 2.)

[2] F. Bobelmann, P. Romano, H. Fabritius, D. Raabe, and M. Epple, “The composition of the exoskeleton of two crustacea: The american lobster homarus americanus and the edible crab cancer pagurus,” *Thermochimica Acta*, vol. 463, no. 1-2, pp. 65–68, 2007. (Cited on page 1.)

[3] D. Raabe, C. Sachs, and P. Romano, “The crustacean exoskeleton as an example of a structurally and mechanically graded biological nanocomposite material,” *Acta Materialia*, vol. 53, no. 15, pp. 4281–4292, 2005. (Cited on pages 1 and 2.)

[4] B. R. Lawn, J. J. W. Lee, and H. Chai, “Teeth: Among nature’s most durable biocomposites,” *Annual Review of Materials Research, Vol 40*, vol. 40, pp. 55–75, 2010. (Cited on page 2.)

[5] B. J. F. Bruet, J. H. Song, M. C. Boyce, and C. Ortiz, “Materials design principles of ancient fish armour,” *Nature Materials*, vol. 7, no. 9, pp. 748–756, 2008. (Cited on page 2.)

[6] D. G. Stavenga, S. Foletti, G. Palasantzas, and K. Arikawa, “Light on the moth-eye corneal nipple array of butterflies,” *Proceedings of the Royal Society B-Biological Sciences*, vol. 273, no. 1587, pp. 661–667, 2006. (Cited on pages 2 and 3.)

[7] W. H. Miller, *Handbook of Sensory Physiology*, vol. VII/6A, pp. 69–143. Springer, 1979. (Cited on page 3.)

[8] A. Yoshida, M. Motoyama, A. Kosaku, and K. Miyamoto, “Antireflective nanoprotuberance array in the transparent wing of a hawkmoth, cephonodes hylas,” *Zoological Science*, vol. 14, no. 5, pp. 737–741, 1997. (Cited on page 3.)

[9] J. Zhong, H. Chen, G. Saraf, Y. Lu, C. K. Choi, J. J. Song, D. M. Mackie, and H. Shen, “Integrated zno nanotips on gan light emitting diodes for enhanced emission efficiency,” *Applied Physics Letters*, vol. 90, no. 20, p. 203515, 2007. (Cited on page 3.)

[10] D. W. Bechert, M. Bruse, W. Hage, J. G. T. VanderHoeven, and G. Hoppe, “Experiments on drag-reducing surfaces and their optimization with an adjustable geometry,” *Journal of Fluid Mechanics*, vol. 338, pp. 59–87, 1997. (Cited on pages 4, 30 and 31.)

[11] B. Dean and B. Bhushan, “Shark-skin surfaces for fluid-drag reduction in turbulent flow: a review,” *Philosophical Transactions of the Royal Society A -Mathematical Physical and Engineering Sciences*, vol. 368, no. 1929, pp. 4775–4806, 2010. (Cited on pages 4 and 31.)

[12] W. Baumgartner, F. Fidler, A. Weth, M. Habbecke, P. Jakob, C. Butenweg, and W. Bohme, “Investigating the locomotion of the sandfish in desert sand using nmr-imaging,” *Plos One*, vol. 3, no. 10, pp. –, 2008. (Cited on page 5.)

[13] I. Rechenberg and A. R. El Khyari, “Solid friction reduction on the skin of the sand-skink.” `http://www.bionik.tu-berlin.de/institut/xs2skink.html`, 2005. Retrieved on December 16, 2010. (Cited on page 5.)

[14] W. Baumgartner, F. Saxe, A. Weth, D. Hajas, D. Sigumonrong, J. Emmerlich, M. Singheiser, W. Bohme, and J. M. Schneider, “The sandfish’s skin: Morphology, chemistry and reconstruction,” *Journal of Bionic Engineering*, vol. 4, no. 1, pp. 1–9, 2007. (Cited on page 5.)

[15] W. Berns, “Sandfish (scincus scincus).” `http://en.wikipedia.org/wiki/File:Apothekerskink01.jpg`, 2005. Retrieved on December 16, 2010. (Cited on page 5.)

[16] K. Autumn and N. Gravish, “Gecko adhesion: evolutionary nanotechnology,” *Philosophical Transactions of the Royal Society A - Mathematical Physical and Engineering Sciences*, vol. 366, no. 1870, pp. 1575–1590, 2008. (Cited on pages 5, 6 and 7.)

[17] D. Campolo, S. D. Jones, and R. S. Fearing, “Fabrication of gecko foot-hair like nano structures and adhesion to random rough surfaces,” in *IEEE Nano 2003*, vol. 2, (San Francisco, CA), pp. 856–859, 2003. (Cited on page 6.)

[18] L. Alibardi, “Ultrastructural autoradiographic and immunocytochemical analysis of setae formation and keratinization in the digital pads of the gecko hemidactylus turcicus (gekkonidae, reptilia),” *Tissue Cell*, vol. 35, pp. 288–296, 2003. (Cited on page 5.)

[19] A. P. Russell, “A contribution to the functional morphology of the foot of the tokay, gekko gecko (reptilia, gekkonidae),” *Journal of Zoology, London*, vol. 176, pp. 437–476, 1975. (Cited on page 6.)

[20] D. J. Irschick, C. C. Austin, K. Petren, R. N. Fisher, J. B. Losos, and O. Ellers, “A comparative analysis of clinging ability among pad-bearing lizards,” *Biological Journal of the Linnean Society*, vol. 59, no. 1, pp. 21 – 35, 1996. (Cited on page 6.)

[21] K. Autumn, M. Sitti, Y. A. Liang, A. M. Peattie, W. R. Hansen, S. Sponberg, T. W. Kenny, R. Fearing, J. N. Israelachvili, and R. J. Full, “Evidence for van der waals adhesion in gecko setae,” *Proceedings of the National Academy of Sciences of the United States of America*, vol. 99, pp. 12252–12256, 2002. (Cited on page 6.)

[22] K. Autumn and A. M. Peattie, “Mechanisms of adhesion in geckos,” *Integrative and Comparative Biology*, vol. 42, pp. 1081–1090, 2002. (Cited on pages 6 and 7.)

[23] K. Autumn, Y. A. Liang, Hsieh, S. T., W. Zesch, W.-P. Chan, W. T. Kenny, R. Fearing, and R. J. Full, “Adhesive force of a single gecko foot-hair,” *Nature*, vol. 405, pp. 681–685, 2000. (Cited on page 7.)

[24] J. Israelachvili, *Intermolecular and surface forces.* New York, NY: Academic Press, 1992. (Cited on page 7.)

[25] A. R. Parker and C. R. Lawrence, “Water capture by a desert beetle,” *Nature*, vol. 414, no. 6859, pp. 33–34, 2001. (Cited on page 7.)

[26] X. F. Gao and L. Jiang, “Water-repellent legs of water striders,” *Nature*, vol. 432, no. 7013, pp. 36–36, 2004. (Cited on page 8.)

[27] Z. Cerman, B. Striffler, and W. Barthlott, *Dry in the water: The superhydrophobic water fern Salvinia - A model for biomimetic surfaces*, ch. 6, p. 97. Berlin Heidelberg: Springer, 2009. (Cited on page 8.)

[28] W. Barthlott, T. Schimmel, S. Wiersch, K. Koch, M. Brede, M. Barczewski, S. Walheim, A. Weis, A. Kaltenmaier, A. Leder, and H. F. Bohn, “The salvinia paradox: Superhydrophobic surfaces with hydrophilic pins for air retention under water,” *Advanced Materials*, vol. 22, no. 21, pp. 2325–2328, 2010. (Cited on pages 8, 9 and 31.)

[29] K. Koch, B. Bhushan, and W. Barthlott, *Multifunctional Plant Surfaces and Smart Materials*, ch. 41, pp. 1399–1436. Springer, 3 ed., 2010. (Cited on pages 9 and 10.)

[30] K. Koch, B. Bhushan, and W. Barthlott, “Multifunctional surface structures of plants: An inspiration for biomimetics,” *Progress in Materials Science*, vol. 54, no. 2, pp. 137–178, 2009. (Cited on pages 10 and 25.)

[31] W. Barthlott and C. Neinhuis, “Purity of the sacred lotus, or escape from contamination in biological surfaces,” *Planta*, vol. 202, no. 1, pp. 1–8, 1997. (Cited on page 10.)

[32] T. S. Chow, “Nanoscale surface roughness and particle adhesion on structures substrates,” *Nanotechnology*, vol. 18, pp. 1–4, 2007. (Cited on page 10.)

[33] P. Hiemenz and R. Rajagopalan, *Principles of colloid and surface chemistry.* CRC Press, 1997. (Cited on pages 11, 12 and 17.)

[34] G. Whyman, E. Bormashenko, and T. Stein, “The rigorous derivation of young, cassie–baxter and wenzel equations and the analysis of the contact angle hysteresis phenomenon,” *Chemical Physics Letters*, vol. 450, no. 4-6, pp. 355–359, 2008. (Cited on page 12.)

[35] R. N. Wenzel, “Resistance of solid surfaces to wetting by water,” *Industrial & Engineering Chemistry*, vol. 28, no. 8, pp. 988–994, 1936. (Cited on page 13.)

[36] A. B. D. Cassie, “Contact angles,” *Discussions of the Faraday Society*, vol. 3, pp. 11–16, 1948. (Cited on page 13.)

[37] B. Bhushan, M. Nosonovsky, and Jun, “Towards optimization of patterned superhydrophobic surfaces,” *Journal of the Royal Society Interface*, vol. 4, pp. 643–648, 2007. (Cited on page 14.)

[38] P. Roach, N. J. Shirtcliffe, and M. I. Newton, “Progess in superhydrophobic surface development,” *Soft Matter*, vol. 4, no. 2, p. 224, 2008. (Cited on pages 15, 25, 26 and 28.)

[39] N. Shirtcliffe, G. McHale, M. Newton, C. Perry, and P. Roach, “Porous materials show superhydrophobic to superhydrophilic switching,” *Chemical Communications*, vol. 25, pp. 3135–3137, 2005. (Cited on page 15.)

[40] M. Nosonovsky, “Multiscale roughness and stability of superhydrophobic biomimetic interfaces,” *Langmuir*, vol. 23, no. 6, pp. 3157–3161, 2007. (Cited on pages 15 and 26.)

[41] Z. Yoshimitsu, A. Nakajima, T. Watanabe, and K. Hashimoto, “Effects of surface structure on the hydrophobicity and sliding behavior of water droplets,” *Langmuir*, vol. 18, no. 15, pp. 5818–5822, 2002. (Cited on page 15.)

[42] D. Quere, “Non-sticking drops,” *Reports on Progress in Physics*, vol. 68, no. 11, pp. 2495–2532, 2005. (Cited on page 15.)

[43] D. Öner and T. J. McCarthy, “Ultrahydrophobic surfaces. effects of topography length scales on wettability,” *Langmuir*, vol. 16, no. 20, pp. 7777–7782, 2000. (Cited on pages 15, 16 and 21.)

[44] C. J. Lv, C. W. Yang, P. F. Hao, F. He, and Q. S. Zheng, “Sliding of water droplets on microstructured hydrophobic surfaces,” *Langmuir*, vol. 26, no. 11, pp. 8704–8708, 2010. (Cited on pages 15 and 16.)

[45] J. Johnson, E. R. and R. H. Dettre, *Contact Angle Hysteresis*, vol. 43, ch. 7, pp. 112–135. American Chemical Society, 1963. (Cited on page 16.)

[46] L. C. Gao and T. J. McCarthy, “The "lotus effect" explained: Two reasons why two length scales of topography are important,” *Langmuir*, vol. 22, no. 7, pp. 2966–2967, 2006. (Cited on pages 16 and 17.)

[47] H.-J. Butt, K. Graf, and M. Kappl, *Physics and chemistry of interfaces.* John Wiley & Sons Canada, 1 ed., 2003. (Cited on page 16.)

[48] Q.-S. Zheng, Y. Yu, and Z.-H. Zhao, “Effects of hydraulic pressure on the stability and transition of wetting modes of superhydrophobic surfaces,” *Langmuir*, vol. 21, no. 26, pp. 12207–12212, 2005. (Cited on pages 17 and 18.)

[49] N. J. Shirtcliffe, G. McHale, M. I. Newton, and C. C. Perry, “Wetting and wetting transitions on copper-based super-hydrophobic surfaces,” *Langmuir*, vol. 21, no. 3, pp. 937–943, 2005. (Cited on page 17.)

[50] G. Erpul, L. D. Norton, and D. Gabriels, “Raindrop-induced and wind-driven soil particle transport,” *Catena*, vol. 47, no. 3, pp. 227 – 243, 2002. (Cited on page 17.)

[51] N. A. Patankar, “Transition between superhydrophobic states on rough surfaces,” *Langmuir*, vol. 20, no. 17, pp. 7097–7102, 2004. (Cited on page 17.)

[52] Y. Yu, “Mechanical and superhydrophobic stabilities of two-scale surfacial structure of lotus leaves,” *Langmuir*, vol. 23, pp. 8212–8216, 2007. (Cited on page 18.)

[53] “Ksv cam 200 optical contact angle/surface tension meter.” `http://www.nlab.pl/KSV/KSV_CAM200.pdf`. Retrieved on December 16, 2010. (Cited on page 19.)

[54] M. Quirk and J. Serda, *Semiconductor Manufacturing Technology.* Prentice-Hall, 2001. (Cited on page 20.)

[55] T. L. Sun, L. Feng, X. F. Gao, and L. Jiang, "Bioinspired surfaces with special wettability," *Accounts of Chemical Research*, vol. 38, no. 8, pp. 644–652, 2005. (Cited on page 22.)

[56] S. Y. Chou, P. R. Krauss, and P. J. Renstrom, "Imprint of sub-25 nm vias and trenches in polymers," *Applied Physics Letters*, vol. 67, no. 21, pp. 3114–3116, 1995. (Cited on page 22.)

[57] M. D. Austin, H. Ge, W. Wu, M. Li, Z. Yu, D. Wasserman, S. A. Lyon, and Chou, "Fabrication of 5nm linewidth and 14nm pitch features by nanoimprint lith," *App*, vol. 84, pp. 5299–5301, 2004. (Cited on page 22.)

[58] H. Schift and A. Kristensen, *Nanoimprint Lithography - Patterning of Resists Using Molding*, ch. 9, pp. 273–312. Springer Handbook of Nanotechnology, Springer, 3 ed., 2010. (Cited on pages 22 and 23.)

[59] F. Mumm, A. T. J. van Helvoort, and P. Sikorski, "Easy route to superhydrophobic copper-based wire-guided droplet microfluidic systems," *Acs Nano*, vol. 3, no. 9, pp. 2647–2652, 2009. (Cited on page 24.)

[60] Y. Lee, K. Y. Ju, and J. K. Lee, "Stable biomimetic superhydrophobic surfaces fabricated by polymer replication method from hierarchically structured surfaces of al templates," *Langmuir*, vol. 26, no. 17, pp. 14103–14110, 2010. (Cited on pages 24 and 25.)

[61] B. Kim, H. Chung, K. S. Chu, H. G. Yoon, C. J. Lee, and W. Kim, "Synthesis of vertically-aligned carbon nanotubes on stainless steel by water-assisted chemical vapor deposition and characterization of their electrochemical properties," *Synthetic Metals*, vol. 160, no. 7-8, pp. 584–587, 2010. (Cited on page 24.)

[62] C. E. Baddour, F. Fadlallah, D. Nasuhoglu, R. Mitra, L. Vandsburger, and J. L. Meunier, "A simple thermal cvd method for carbon nanotube synthesis on stainless steel 304 without the addition of an external catalyst," *Carbon*, vol. 47, no. 1, pp. 313–318, 2009. (Cited on pages 24 and 25.)

[63] C. Masarapu and B. Q. Wei, "Direct growth of aligned multiwalled carbon nanotubes on treated stainless steel substrates," *Langmuir*, vol. 23, no. 17, pp. 9046–9049, 2007. (Cited on page 24.)

[64] N. Ishigami, H. Ago, K. Imamoto, M. Tsuji, K. Iakoubovskii, and N. Minami, "Crystal plane dependent growth of aligned single-walled carbon nanotubes on sapphire," *Journal of the American Chemical Society*, vol. 130, no. 30, pp. 9918–9924, 2008. (Cited on page 25.)

[65] N. J. Shirtcliffe, G. McHale, M. I. Newton, and C. C. Perry, "Intrinsically superhydrophobic organosilica sol-gel foams," *Langmuir*, vol. 19, no. 14, pp. 5626–5631, 2003. (Cited on page 26.)

[66] P. S. Tsai, Y. M. Yang, and Y. L. Lee, "Fabrication of hydrophobic surfaces by coupling of langmuir-blodgett deposition and a self-assembled monolayer," *Langmuir*, vol. 22, no. 13, pp. 5660–5665, 2006. (Cited on page 26.)

[67] L. Q. Zhu and Y. Jin, "A novel method to fabricate water-soluble hydrophobic agent and super-hydrophobic film on pretreated metals," *Applied Surface Science*, vol. 253, no. 7, pp. 3432–3439, 2007. (Cited on page 26.)

[68] C. Neinhuis and W. Barthlott, "Characterization and distribution of water-repellent, self-cleaning plant surfaces," *Annals of Botany*, vol. 79, no. 6, pp. 667–677, 1997. (Cited on page 26.)

[69] Y. Li, X. J. Huang, S. H. Heo, C. C. Li, Y. K. Choi, W. P. Cai, and S. O. Cho, "Superhydrophobic bionic surfaces with hierarchical microsphere/swcnt composite arrays," *Langmuir*, vol. 23, no. 4, pp. 2169–2174, 2007. (Cited on page 26.)

[70] Y. C. Jung and B. Bhushan, "Mechanically durable carbon nanotube-composite hierarchical structures with superhydrophobicity, self-cleaning, and low-drag," *Acs Nano*, vol. 3, no. 12, pp. 4155–4163, 2009. (Cited on pages 26 and 30.)

[71] B. Bhushan, "Biomimetics: lessons from nature - an overview," *Philosophical Transactions of the Royal Society A - Mathematical Physical and Engineering Sciences*, vol. 367, pp. 1445–1486, APR 28 2009. (Cited on page 27.)

[72] S. Corp., "Stocoat lotusan." `http://www.stocorp.com/index.php/en/20090714306/videos-product/sto-videos/menu-id-271.html`. Retrieved on December 16, 2010. (Cited on page 27.)

[73] J. Xiong, S. N. Das, B. Shin, J. P. Kar, J. H. Choi, and J. M. Myoung, "Biomimetic hierarchical zno structure with superhydrophobic and antireflective properties," *Journal of Colloid and Interface Science*, vol. 350, no. 1, pp. 344–347, 2010. (Cited on page 28.)

[74] L. Mishchenko, B. Hatton, V. Bahadur, J. A. Taylor, T. Krupenkin, and J. Aizenberg, "Design of ice-free nanostructured surfaces based on repulsion of impacting water droplets, *published online*," *ACS Nano*, no. 0, 2010. (Cited on pages 28 and 29.)

[75] U. G. Survey, "Gas hydrate: What is it?." `http://woodshole.er.usgs.gov/project-pages/hydrates/what.html`, 2009. Retrieved on December 16, 2010. (Cited on page 29.)

[76] M. D. Max, *Natural Gas Hydrate in Oceanic and Permafrost Environments.* Kluwer Academic Publishers, 2003. (Cited on page 30.)

[77] Y. C. Jung and B. Bhushan, "Biomimetic structures for fluid drag reduction in laminar and turbulent flows," *Journal of Physics - Condensed Matter*, vol. 22, pp. 1–9, 2009. (Cited on pages 30 and 31.)

[78] V. Eyring, H. W. Kohler, J. van Aardenne, and A. Lauer, "Emissions from international shipping: 1. the last 50 years," *Journal of Geophysical Research-Atmospheres*, vol. 110, no. D17, pp. –, 2005. (Cited on page 30.)

[79] B. Bhushan, ed., *Springer Handbook of Nanotechnology.* Heidelberg: Springer, 2 ed., 2007. (Cited on page 30.)

[80] O. Geschke, K. H., and P. Telleman, eds., *Microsystem Engineering of Lab on a Chip Devices.* Wiley VCH, 2 ed., 2008. (Cited on page 30.)

[81] J. N. A. Matthews, "Low-drag suit propels swimmers," *Physics Today*, vol. 61, no. 8, pp. 32–33, 2008. (Cited on page 31.)

[82] G. K. Batchelor, *An Introduction to Fluid Dynamics.* Cambridge: Cambridge University Press, 1970. (Cited on page 31.)

[83] Y. Wang, B. Bhushan, and A. Maali, "Atomic force microscopy measurement of boundary slip on hydrophilic, hydrophobic, and superhydrophobic surfaces," *Journal of Vacuum Science & Technology*, vol. 27, pp. 754–760, 2009. (Cited on page 31.)

[84] T. Liu, Y. Yin, S. Chen, X. Chang, and S. Cheng, "Super-hydrophobic surfaces improve corrosion resistance of copper in seawater," *Electrochimica Acta*, vol. 52, no. 11, pp. 3709 – 3713, 2007. (Cited on page 31.)

[85] L. Zhai, M. C. Berg, F. c. Cebeci, Y. Kim, J. M. Milwid, M. F. Rubner, and R. E. Cohen, "Patterned superhydrophobic surfaces: Toward a synthetic mimic of the namib desert beetle," *Nano Letters*, vol. 6, no. 6, pp. 1213–1217, 2006. PMID: 16771582. (Cited on page 31.)

Appendix A

Nanoindentation Lab Exercise

TKT4146 Nanomechanics
Lab Exercise I

Thor Christian Hobæk

9th December 2010

1 Introduction

Nanoindentation is an instrument designed to measure mechanical properties of materials with submicron-precision. It uses a hard and small tip, whose mechanical properties and geometrical shape is well known (for instance the Berkovich tip). While indenting, it can measure the load and depth simultaneously, giving a load-displacement hysteresis for a loading-unloading cycle. From these data-points, useful material parameters can be extracted.

Two frequently measured mechanical parameters measured with the nanoindenter is the hardness H, given as

$$H = \frac{P_{max}}{A} \tag{1}$$

and the elastic modulus E, given by

$$\frac{1}{E_r} = \frac{(1-\nu^2)}{E} + \frac{(1-\nu_i^2)}{E_i} \tag{2}$$

E_r is defined as

$$E_r = \frac{\sqrt{\pi}}{2}\frac{S}{\sqrt{A}} \tag{3}$$

where the experimentally measured stiffness S is given as the linear slope of the initial portion of the unloading curve

$$S = \frac{dP}{dh} \tag{4}$$

and the contact area A estimated at the contact depth h_c at the perimeter of the Berkovich indenter is given by

$$A = 24.5h_c^2 + 6.83h_c - 3.09h_c^{1/2} + 2.05h_c^{1/4} - 3.26h_c^{1/8} + 1.37h_c^{1/16} \tag{5}$$

The first term in this equation describes the contact area of a perfect Berkovich shape, the other terms are calculated during calibrations to compensate for blunting and imperfections of the tip. However, the perimeter contact depth h_c can not be read off from the load-displacement curve directly. One can determine h_s, the displacement of material from the surface to the perimeter of the tip given by

$$h_s = \epsilon \frac{P_{max}}{S} \tag{6}$$

where $\epsilon = 0.75$ is the geometrical constant for the Berkovich tip. The total displacement of sample from the initial height to the tip of the indenter at the end of the loading must be given by

$$h_{max} = h_c + h_s \tag{7}$$

so that

$$h_c = h_{max} - h_s \tag{8}$$

Thus, the contact area can finally be calculated and inserted into equation 1 and 2 along with P_{max} and S, which can be directly read of from the load-displacement curve.

2 Experiment

Nanoindentation measurements were conducted for steel and crab skeleton. In this report, only one indentation from the crab skeleton will be presented. The crab skeleton were dried in air and embedded in epoxy and leaving it to cure for 24h. After curing, the samples were polished mechanically using sandpaper starting with a grit size of 240, followed by grit sizes of 550, 800 and 1200. Finally the sample were polished using diamond suspensions down to 1 μm.

Figure 2 shows the cross-section of the crab skeleton embedded in epoxy. Five indentations were made across the junction between the exoskeleton and endoskeleton (the dark and brigth regions).

Figure 2 shows one of the load-displacement curves, where the upper region of the unloading curve has been fitted with a linear function.

With these results and using the formulas in section 1, the mechanical parameters were evaluated and the results are listed in table 1.

3 Discussion

As there is a large scattering in the mechanical properties of biological materials, no conclusion can be drawn from only a single indentation. Also,

Table 1: Calculated mechanical properties of the crab skeleton

Parameter	Value	Unit
S	11.8	$^{kN}/_{m}$
h_{max}	88.9	nm
P_{max}	200.0	μN
h_s	12.7	nm
h_c	76.2	nm
A	0.143	μm^2
H	1.4	GPa
E_r	27.7	GPa

the mechanical properties of crab exoskeletons largely depend on the degree of hydration [1]. Therefore, it would be interesting to test several samples to get a statistical significant result, as well as to investigate the impact of hydration.

References

[1] S. Nikolov et al. Revealing the design principles of high-performance biological composites using ab initio and multiscale simulations: The example of lobster cuticle. *Advanced Materials*, 21:1/8, 2009.

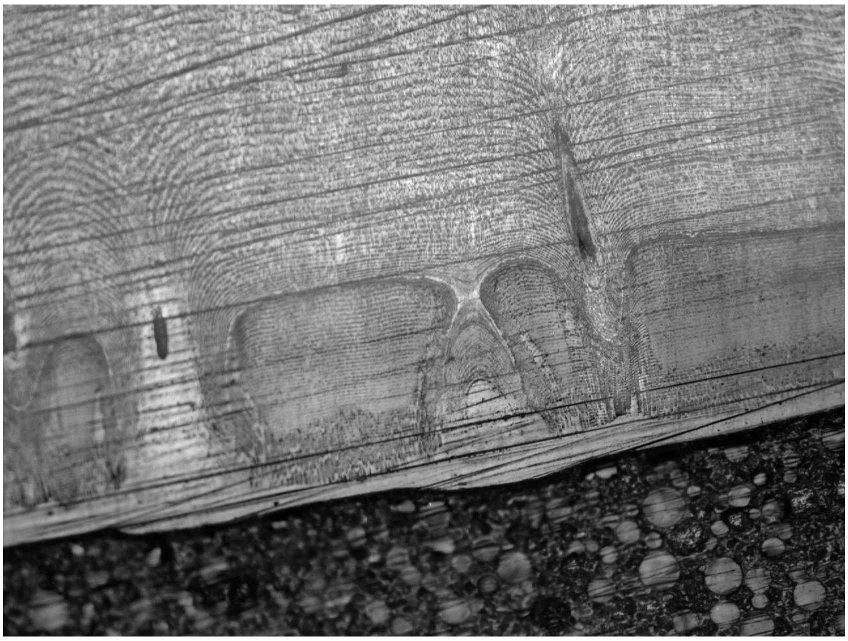

Figure 1: Optical image of the crab skeleton cross-section embedded in epoxy (10x magnification)

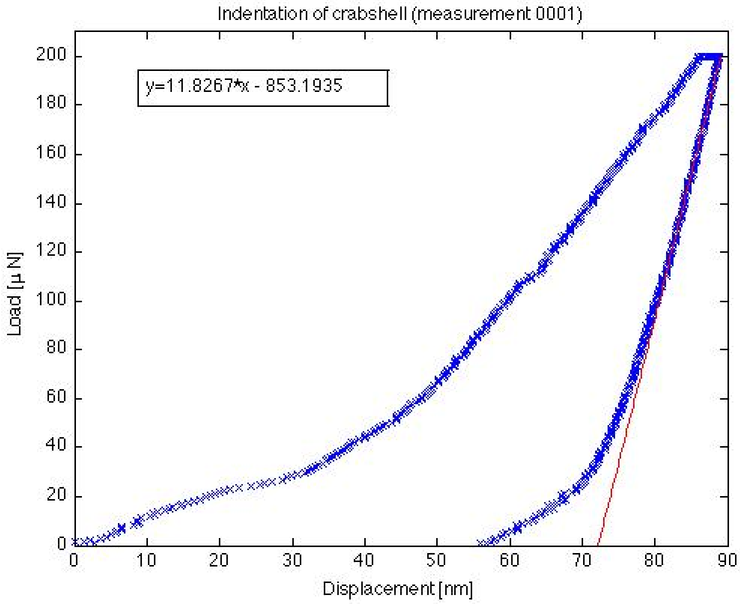

Figure 2: Load-displacement curve showing load-unloading hysteresis. Upper region of unloading curve is fitted with a linear curve to estimate S

Appendix B

Molecular Dynamics Report I

Calculation of Si elastic properites

Molecular dynamics report

Thor Christian Hobæk

November 20, 2010

1 Introduction

The stress-strain relation for 3D strain can be written in matrix notation,

$$\begin{pmatrix}\sigma_1\\ \sigma_2\\ \sigma_3\\ \sigma_4\\ \sigma_5\\ \sigma_6\end{pmatrix} = \begin{pmatrix} C_{11} & C_{12} & C_{13} & C_{14} & C_{15} & C_{16}\\ C_{21} & C_{22} & C_{23} & C_{24} & C_{25} & C_{26}\\ C_{31} & C_{32} & C_{33} & C_{34} & C_{35} & C_{36}\\ C_{41} & C_{42} & C_{43} & C_{44} & C_{45} & C_{46}\\ C_{51} & C_{52} & C_{53} & C_{54} & C_{55} & C_{56}\\ C_{61} & C_{62} & C_{63} & C_{64} & C_{65} & C_{66} \end{pmatrix} \begin{pmatrix}\epsilon_1\\ \epsilon_2\\ \epsilon_3\\ \epsilon_4\\ \epsilon_5\\ \epsilon_6\end{pmatrix}$$

For a cubic crystal system, it follows by symmetry that the stiffness tensor C can be written as

$$C = \begin{pmatrix} C_{11} & C_{12} & C_{12} & 0 & 0 & 0\\ C_{12} & C_{11} & C_{12} & 0 & 0 & 0\\ C_{12} & C_{12} & C_{11} & 0 & 0 & 0\\ 0 & 0 & 0 & C_{44} & 0 & 0\\ 0 & 0 & 0 & 0 & C_{44} & 0\\ 0 & 0 & 0 & 0 & 0 & C_{44} \end{pmatrix}$$

where $C_{11} = C_{22} = C_{33}$, $C_{12} = C_{13} = C_{23}$, $C_{44} = C_{55} = C_{66}$.

The stiffness tensor can be used to calculate Young's modulus E, Poisson's ratio ν, the bulk modulus κ and the shear modulus G. Three crystal models, the Reuss (assuming homogenous stress), Voigt (assuming homogenous strain) and Kroener model (assuming anisotropical spherical single crystal grain in homogenous polycrystalline matrix) will be used to evaluate these constants for single crystal and nanocrystalline Si, using different potentails.

2 Experimental

The mechanical properties of Si were calculated through molecular dynamics (MD) simulations using LAMMPS on Mac OS X v. 10.5.8. First, the example file in.elastic were used as a template to calculate the stress tensor of the silicon. The stress tensor were calculated for single crystal silicon using both Stillinger-Weber potential and Tersoff-Brenner potential by changing the potential in potential.mod. In polycrystalline materials, the atomic configuration is not ideal as in perfect single crystals where the atoms stay at the minimum-energy position. For nanocrystalline silicon, annealing of the system is one way to allow the atoms to settle at the minimum energy. The annealing is done by increasing the temperature from 10 K to 1800 K. The system is then quenched back to 10 K and the atomic configuration is minimized. A dump-file is then written which can be read by the in.elastic example script, replacing the single crystal box structure.

Two different models for the polycrystalline system are used to calculate the elastic constants, Reuss model using homogenous stress and Kröner model with the crystal regions as an anisotropic sphere in homogenous matrix. The elastic constants are calculated by the script and presented in the results section.

3 Results

3.1 Single crystal Si

Using the Stillinger-Weber potential, the following elastic constants were calculated:

$$C_{Si,sw} = \begin{pmatrix} 151.4 & 76.4 & 76.4 & 0 & 0 & 0 \\ & 151.4 & 76.4 & 0 & 0 & 0 \\ & & 151.4 & 0 & 0 & 0 \\ & & & 56.4 & 0 & 0 \\ & & & & 56.4 & 0 \\ & & & & & 56.4 \end{pmatrix}$$

When switching to the Tersoff-Brenner potential, the elastic constants for the same crystal structure were calculated as:

$$C_{Si,tersoff} = \begin{pmatrix} 121.7 & 85.8 & 85.8 & 0 & 0 & 0 \\ & 121.7 & 85.8 & 0 & 0 & 0 \\ & & 121.7 & 0 & 0 & 0 \\ & & & 10.3 & 0 & 0 \\ & & & & 10.3 & 0 \\ & & & & & 10.3 \end{pmatrix}$$

3.2 Nanocrystalline Si

Using Stillinger-Weber potential, the elastic constants were calculated to be

$$C_{NanoSi,sw} = \begin{pmatrix} 158.7 & 93.5 & 94.6 & -0.4 & -0.5 & 1.0 \\ & 159.6 & 93.8 & -1.7 & -0.9 & -3.3 \\ & & 157.3 & 0.6 & 1.6 & 1.1 \\ & & & 31.4 & 0.8 & -0.8 \\ & & & & 31.6 & 0.3 \\ & & & & & 30.8 \end{pmatrix}$$

for the nanocrystalline Si structure.

Using Tersoff potential, the elastic constants were calculated to be

$$C_{NanoSi,tersoff} = \begin{pmatrix} 86{,}5 & 81{,}9 & 58{,}8 & 13{,}3 & -11{,}0 & 7{,}5 \\ & 108{,}3 & 78{,}7 & -11{,}1 & 9{,}6 & -4{,}3 \\ & & 85{,}6 & 13{,}1 & 0{,}6 & -6{,}1 \\ & & & 0{,}2 & -2{,}6 & 9{,}5 \\ & & & & -16{,}1 & 17{,}5 \\ & & & & & -4{,}6 \end{pmatrix}$$

3.3 Mechanical properties

Using equation (1)-(5), the mechanical properties of single crystal and nanocrystalline silicon were calculated using the Stillinger-Weber and the Tersoff potential and summarized in table 1.

4 Discussion

Table 1 summarizes the calculated elastic constants using the stiffness tensor computed by MD-simulations and the Reuss model, the Voigt model and the Kroener model. The stiffness tensor of single crystal silicon deduced from experimental results [1] are shown below

$$C_{Si,exp} = \begin{pmatrix} 165{,}78 & 63{,}94 & 63{,}94 & 0 & 0 & 0 \\ & 165{,}78 & 63{,}94 & 0 & 0 & 0 \\ & & 165{,}78 & 0 & 0 & 0 \\ & & & 79{,}62 & 0 & 0 \\ & & & & 79{,}62 & 0 \\ & & & & & 79{,}62 \end{pmatrix}$$

Table 1: Mechanical properties of Si

Elastic constants							
Crystal structure	Potential	Model	A	$E[GPa]$	$\nu[GPa]$	$\kappa[GPa]$	$G[GPa]$
Single crystal	Stillinger-Weber	Reuss	1,51	122,0	0,299	101,4	47,0
		Voigt	1,51	126,3	0,292	101,4	48,9
		Kroener	1,51	78,3	0,371	101,4	28,6
		Isotropic	1,00	100,2	0,335	101,4	37,5
	Tersoff	Reuss	0,57	35,8	0,439	97,8	12,4
		Voigt	0,57	38,3	0,435	97,8	13,4
		Kroener	0,57	30,8	0,448	97,8	10,6
		Isotropic	1,00	50,7	0,414	97,8	32,3
Nanocrystalline	Stillinger-Weber	Reuss	0,97	87,0	0,374	115,5	31,7
		Voigt	0,97	87,1	0,374	115,5	31,7
		Kroener	0,97	62,9	0,409	115,5	22,3
		Isotropic	1,00	88,6	0,372	115,5	32,3

These constants can be used to calculate the elastic properties using the previously used models and the results are summarized in table 2 together with the known mechanical properties. It can be seen, that the closest model to the experimental values are the Reuss model and the Voigt model, as they most closely matches the elastic modulus and Poisson's ratio that are derived directly from the stiffness tensor. Now, looking at table 1, it can be seen that Stillinger-Weber is a more accurate potential than Tersoff for estimating the mechanical properties of single crystal silicon. This may be due to the fact that Tersoff is developed for treating heteronuclear bonds in materials like SiC.

For nanocrystalline silicon, only the Stillinger-Weber gave realistic values, as the stiffness tensor calculated using Tersoff shows a very low degree of symmetry. As the calculated anisotropical factor is close to 1, the nanocrystalline system closely exhibits isotropic behaviour. Compared to single crystal Si, the elastic modulus and the shear modulus are lower for the nanocrystalline system, while Poisson's ratio and the bulk modulus are higher.

Finally, it could be commented that a more appropriate potential for simulating semiconductor materials like silicon would be MEAM (Modified Embedded Atom Model) or ReaxFF. However, there were some problems in the installation of a gfortran compiler, so these potentials could not be used on the current operating system at this stage.

5 Conclusion

The elastic properties of single crystal and nanocrystalline silicon was determined by MD-simulations and analyzed according to the Reuss, Voigt and Kroener model. These values was compared to experimental values and it was found that the Stillinger-Weber potential

Table 2: Mechanical properties of Si (experimental)

Elastic constants							
Crystal structure	Potential	Model	A	$E[GPa]$	$\nu[GPa]$	$\kappa[GPa]$	$G[GPa]$
Single crystal	Stillinger-Weber	Reuss	1,56	159,6	0,228	97,9	65,0
		Voigt	1,56	165,9	0,217	97,9	68,1
		Kroener	1,56	67,4	0,385	97,9	24,3
		Isotropic	1,00	130,2	0,278	97,9	50,9
		Experimental	1,56	185	0,28	100	52

resembled these values more closely than the Tersoff potential. Also the nanocrystalline silicon showed ”softer” behaviour compared to the single crystal. Results more realistic to experimental values could probably be obtained by using the MEAM or ReaxFF potential.

References

[1] Wikipedia, “Silicon.”

Appendix C

Molecular Dynamics Report II

Mechanics of nanorods

Final report - TKT4146 Nanomechanics

Thor Christian Hobæk

16th December 2010

Abstract

Metallic nanowires are interesting due to their electronic, optical, mechanical and magnetic properties, and are an emerging field of research due to the many potential applications. Molecular dynamics is a useful tool to study mechanical behaviour of nanowires, something which can be challenging using experimental methods due to the tiny length scales involved. In this report, the mechanics of nickel nanowires was examined with respect to size-effect, temperature and strain rate using the embedded atom model (EAM). In addition, the true stress-strain relation was calculated and compared to the engineering stress. Finally, mechanics of nanowires made of copper and gold were also investigated and compared to nickel.

1 Introduction

In the recent years, nanometer-sized structures have achieved a lot of attention due to its mechanical, electrical, optical and magnetic properties. Nanowires can be defined as structures having a diameter of less than 100 nm, while the length is not constrained, thus they are said to be 1-D nanostructures. Metallic nanowires have a huge potential in being used as interconnections and photonic waveguides in electronic, optical and nanomechanical devices. In addition, metallic nanowires have been used as catalysts, superconductors, nanoprobes and as reinforcing fibers in lightweight composite materials [1]. To develop nanomechanical devices using nanowires, it is very important to understand their mechanical behaviour and the dependence upon length scale, deformation rate and temperature. Because of the tiny dimensions of the nanowires, it is very challenging to do mechanical testing experimentally. Thus, molecular dynamics simulations is useful as an alternative to study the nanowire mechanics. In this report, I will examine the mechanics of nickel, copper and gold nanorods using the Embedded-atom method (EAM) to simulate tension and compression, the effect of size, strain-rate, temperature and compare true stress-strain against engineering stress-strain curves.

2 Methods

Mechanical behaviour of metallic Ni nanorods are examined in this report by using Molecular Dynamics (MD) simulations running on the LAMMPS Molecular Dynamics Simulator on a Mac OS X v. 10.5.8 operating platform. Two input files are required for the simulations;

in.equil and *in.nanorod*. The file *in.equil* sets up a system that is periodic in the z-direction and non-periodic and shrink-wrapped in the x and y direction. It then defines a lattice box with boundaries defined in Ångström; -3 < x < 3, -3 < y < 3 and -10 < z < 10, containing coarse-grained atoms arranged ass face-centered cubic (FCC) with lattice parameter $a = 3.470$ Å. The interatomic potential for Ni atoms is then defined according to the Embedded Atom Method (EAM) with parameters given by Foiles *et. al.* [2]. The EAM model is particularly suitable for metallic systems. In this model, the potential energy of an atom i is given by

$$E_i = F_\alpha \left(\sum_{i \neq j} \rho_\beta(r_{ij}) \right) + \frac{1}{2} \sum_{i \neq j} \phi_{\alpha\beta}(r_{ij}) \tag{1}$$

where r_{ij} is the distance between atoms i and j, $\phi_{\alpha\beta}$ is a pair-wise potential function, ρ_β is the contribution to the electron charge density from atom j of type β at the location of atom i, and F is an embedding function that represents the energy required to place atom i of type α into the electron cloud [3].

Then, the ensemble of initial velocities of the atoms are set using a Gaussian distribution with a mean at 0 and standard deviation according to a temperature of 10 K and a zeroed linear and angular momentum. Finally the input-file is equilibrated at 10 K by using the nvt and npt-ensemble respectively, and a restart-file are written at the end.

The restart-file is then read by the input-file *in.nanorod*. This script does either a tension or compression test depending on what is desired. By default, the strain is set to 1.5 for tension and 0.7 for compression. The script finally dumps information about the total, kinetic and potential energy, the external pressure, the pressure tensor in the xx, yy and zz-direction, the box length in the 3 dimensions and the total volume of the box. The thermodynamical data are dumped every 100 picoseconds.

To calculate the engineering stress-strain behaviour, the cross-sectional area at the necking region have to be calculated simultaneously as the nanowire deforms. This is achieved by defining a box spanning the length of the nanorod in the x- and y-direction and constrained between -3 Å < z < 3 Å. The area in the xy-plane is calculated by a user-defined function.

From the simulation output data, the stress-strain relationship and the elastic constants of the nanorod can be evaluated. Furthermore, the simulation results was visualized from the dump-file using Ovito for Mac OS X to explain the deformation process of the nickel nanorod under tension and compression.

3 Results

3.1 Tension and compression tests of Ni nanorod

Stress-strain relations for tension and compression were obtained for Ni nanorods formed as a cubic box with initial dimensions of 21.3 Å x 21.3 Å x 69.4 Å. Figure 1 shows the engineering stress-strain relations of the Ni nanorod under tension (assuming constant cross-sectional area in the x- and y-direction). It shows an elastic region where the stress-strain relation is linear, until the strain reaches about 12%. At this point, there is a sharp drop in the stress, which indicates that yielding occurs and that the nanorod is now deformed plastically. After this point, the stress increases a bit before a small drop before 50% elongation, but it does not actually fracture during the test.

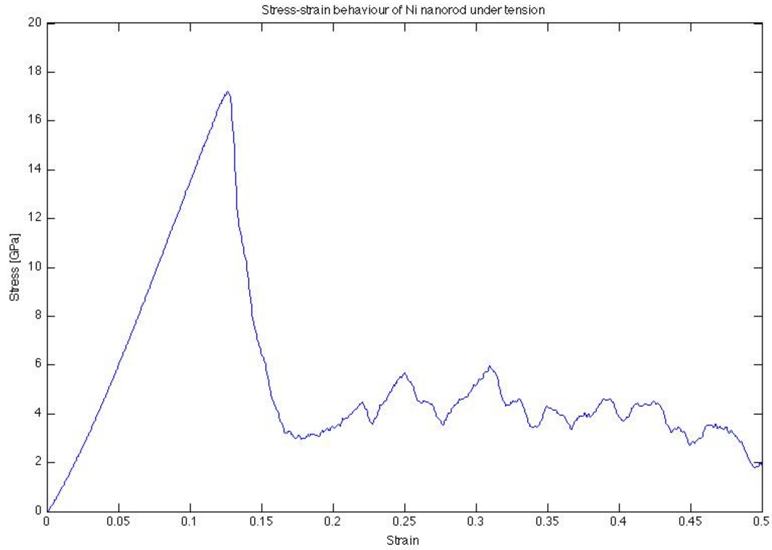

Figure 1: Stress-strain relationship for nickel nanorod under tension

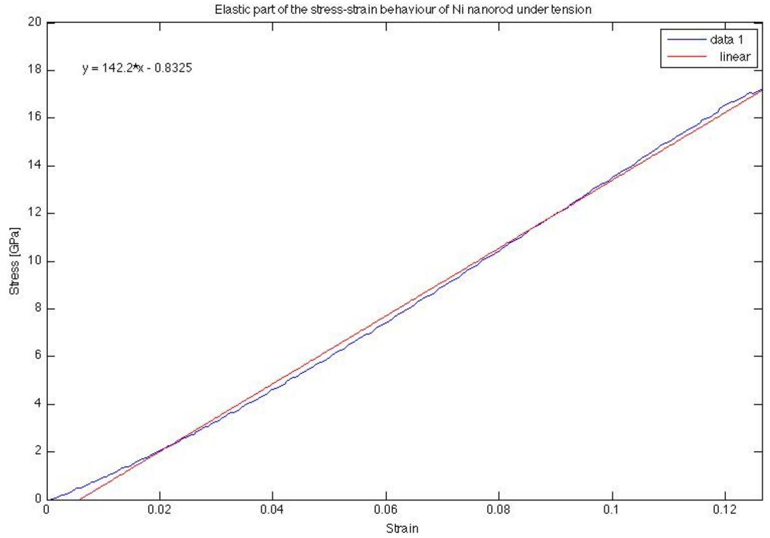

Figure 2: Elastic portion of the stress-strain relationship for nickel nanorod under tension, with linear fitting to estimate Young's modulus

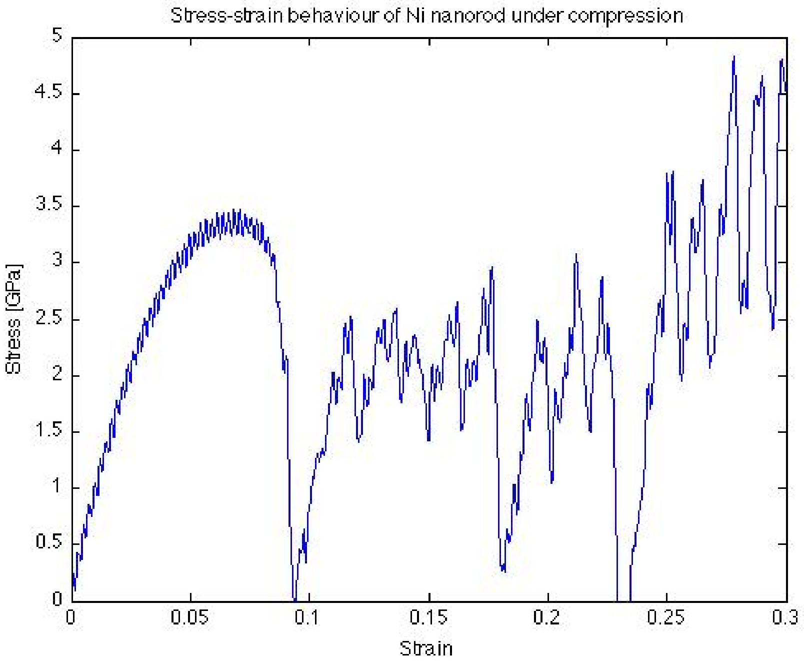

Figure 3: Stress-strain relationship for nickel nanorod under compression

Figure 2 shows the elastic range of figure 1, where the stress-strain relationship has been fitted by linear regression to estimate Young's modulus to $E = 142.2$ GPa for tension.

Figure 3 shows the stress-strain relationship under compression for the same Ni nanorod. The yielding point is at about 8%, where the plastic deformation starts. The sharp drops in stress after this point shows that dislocation occurs through slip planes.

The elastic range of the compressive stress-strain relation is plotted in the same way as with the tensile test. The compressive elastic modulus is estimated to be $E = 81.8$ GPa

Figure 5 shows a sequence of snapshots taken during the tensile deformation of the Ni nanorod under tension, visualised using Ovito. It shows that the deformation is elastic in the two first snapshots, while for the next three snapshots the nanorod deforms plastically. One can also see the necking process at these last three sequences as the cross-sectional area decreases with increasing strain. Due to the necking, the stress concentration is quite high in this region and this effect will be discussed further in section 4.5.

Figure 6 shows the deformation process under compression. It shows formation of dislocation planes on the third snapshot and onwards.

3.2 Size effects

To examine the size effects, nanorods with 2 and 3 times the initial length were simulated using the *replicate* command. The resulting stress-strain relation is compared in figure 7. All three lengths show the same elastic behaviour, but the plastic deformation is a bit different with earlier fracture of the longer nanorods.

Figure 8 shows a comparison of the two nanorods under compression. As both curves show similar mechanical behaviour, there is a very small size effect on compression.

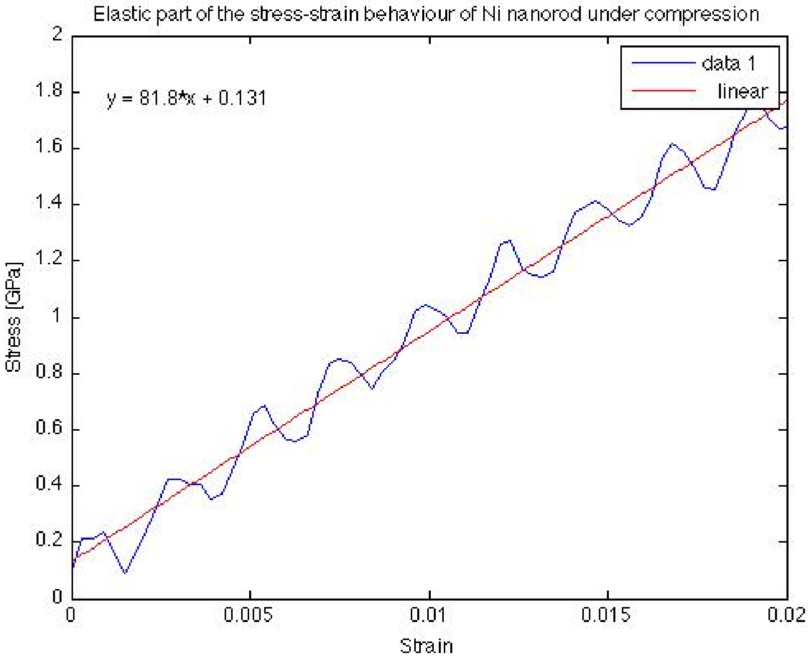

Figure 4: Elastic portion of the stress-strain relationship for nickel nanorod under compression, with linear fitting to estimate Young's modulus

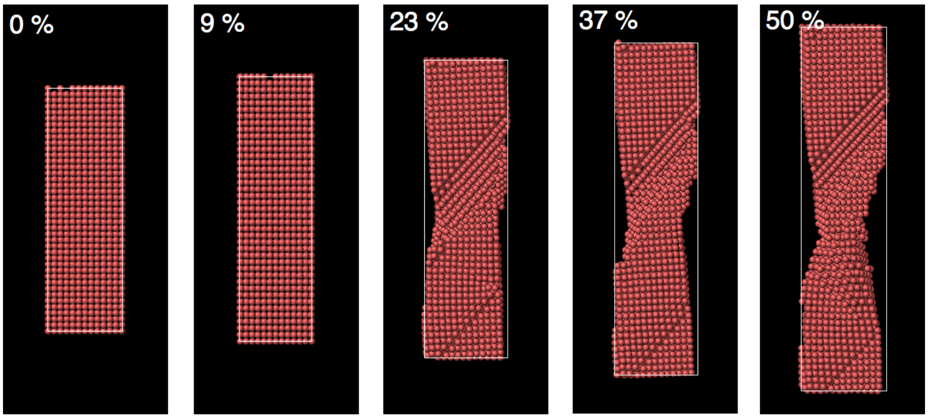

Figure 5: Snapshot sequence of the tensile deformation of the Ni nanorod visualised by Ovito

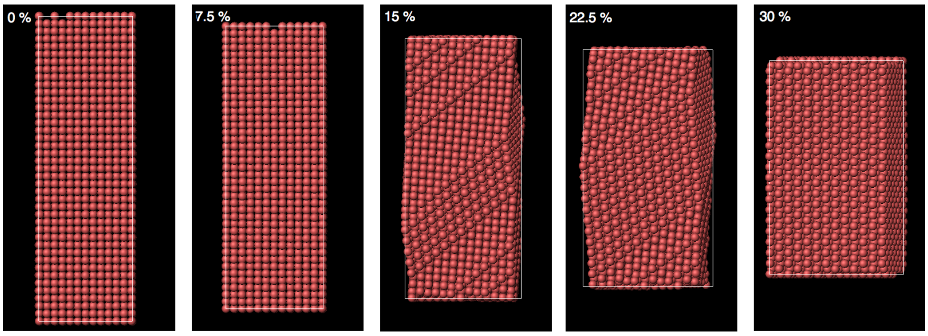

Figure 6: Snapshot sequence of the compressive deformation of the Ni nanorod visualised by Ovito

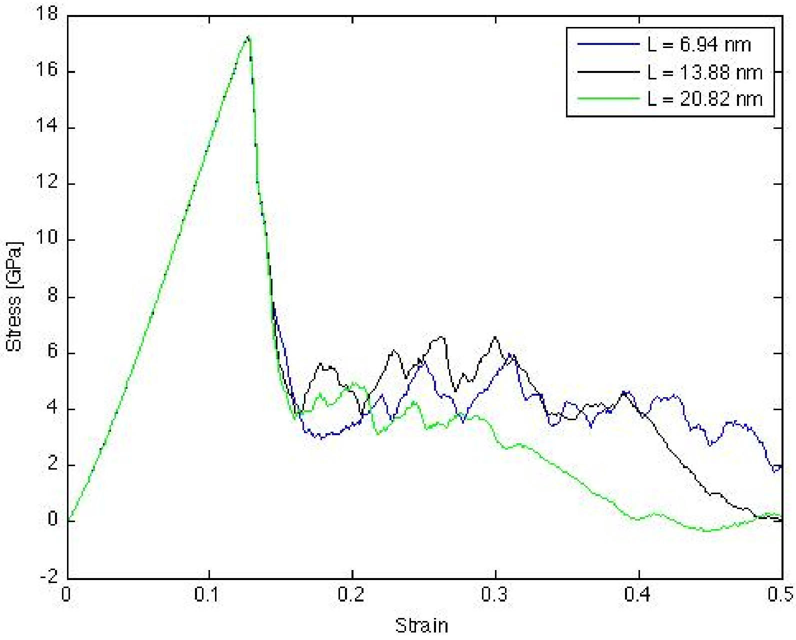

Figure 7: Stress-strain relations of nanorods under tension with two different lengths

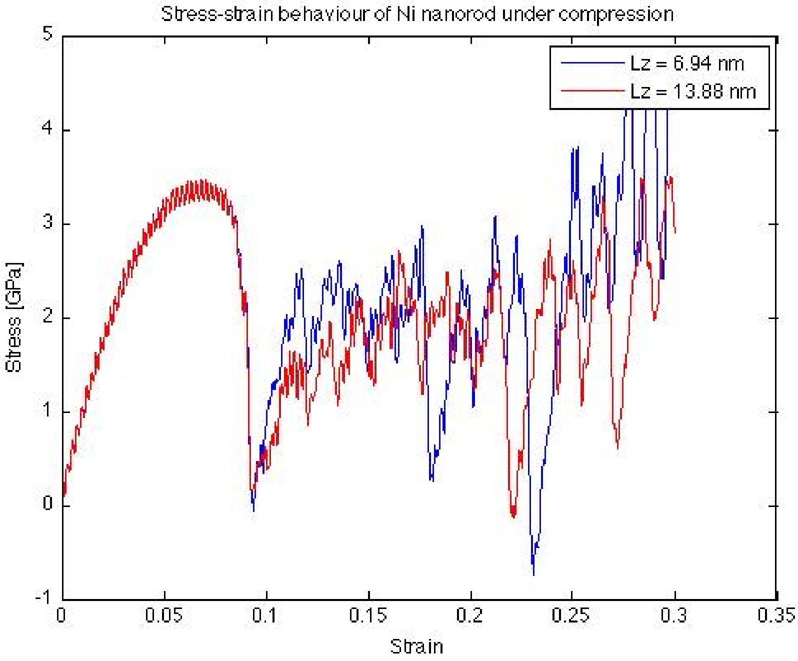

Figure 8: Stress-strain relations of nanorods under compression with two different lengths

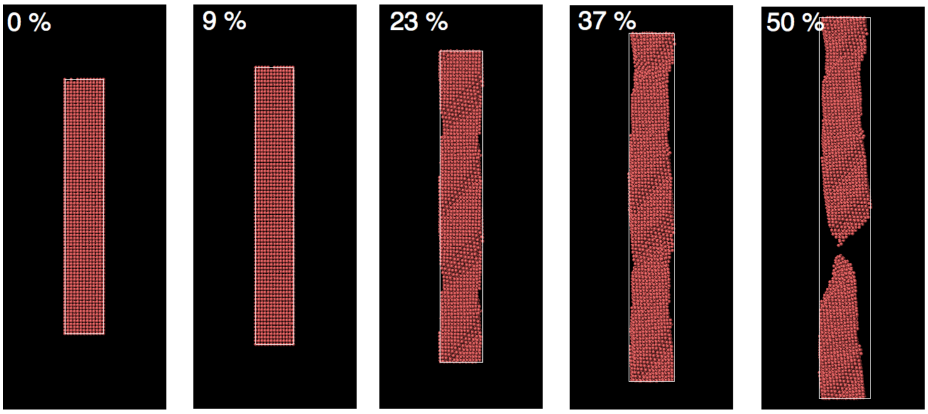

Figure 9: Snapshot of the twice as large Ni nanorod under tension. Compared to figure 5, the necking process is more pronounced and at the end of the sequence, complete fracture occurs.

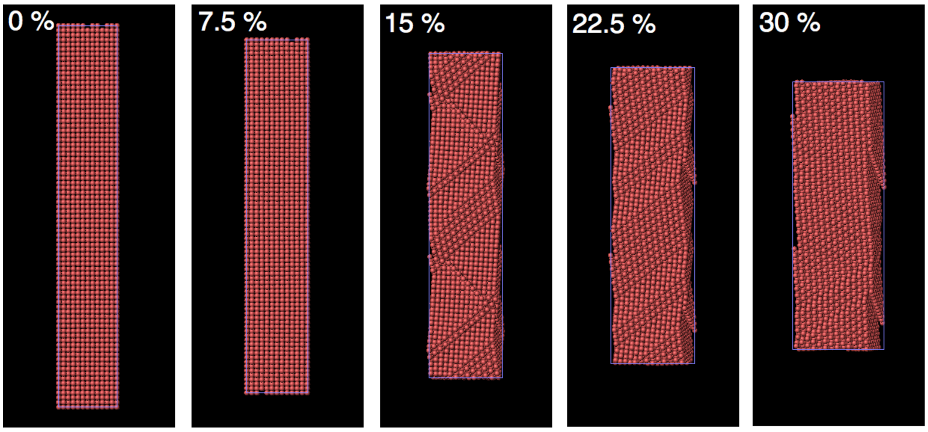

Figure 10: Snapshot of the twice as large Ni nanorod under compression

Figure 9 shows the sequence of snapshots for the larger nanorod under tension. Compared to figure 5, the necking is more pronounced and it can be seen that complete fracture occurs at 50% strain. For compression shown in figure 10, the same kind of behaviour can be seen as for the shorter nanorod in 6.

3.3 Strain rate dependance

Figure 11 shows tensile tests of the nickel nanorod with different strain rates. It shows that the elastic modulus is almost independent on the strain rate. However, larger strain rates leads to a higher yield strength and a larger resistance towards deformation than for lower strain rates. Because the yield strength seems to depend on the strain rate, the resulting values were plotted on a semilog scale, see figure 12.

3.4 Temperature dependance

Figure 13 shows tensile tests of the Ni nanorod at different temperatures. It shows that at room temperature, the nanorod becomes softer and is easier to deform than at 10 K. The elastic modulus at $T = 300$ K is also estimated to be 114.8 GPa compared to 142.8 GPa at $T = 10$ K.

3.5 Calculating the true stress-strain relation

While calculation of the engineering stress-strain assumes a constant cross-sectional area, one has to take the change in this area during deformation into considering. This is especially important when necking occurs. To update the change in cross-section each timestep, a region confining the region the centre of the rod bounded by -3 Å$< z <$ +3 Å. Figure 15 shows the change in the cross-section for the whole box (blue curve) compared to the change in cross-section for the central region (red curve). It is observed that both lines are very similar during the elastic region, but when the deformation enters the plastic region, the blue line increases while the red line decreases. This is a sign that necking actually occurs and that this change have to be taken into consideration when calculating the true stress-strain relation.

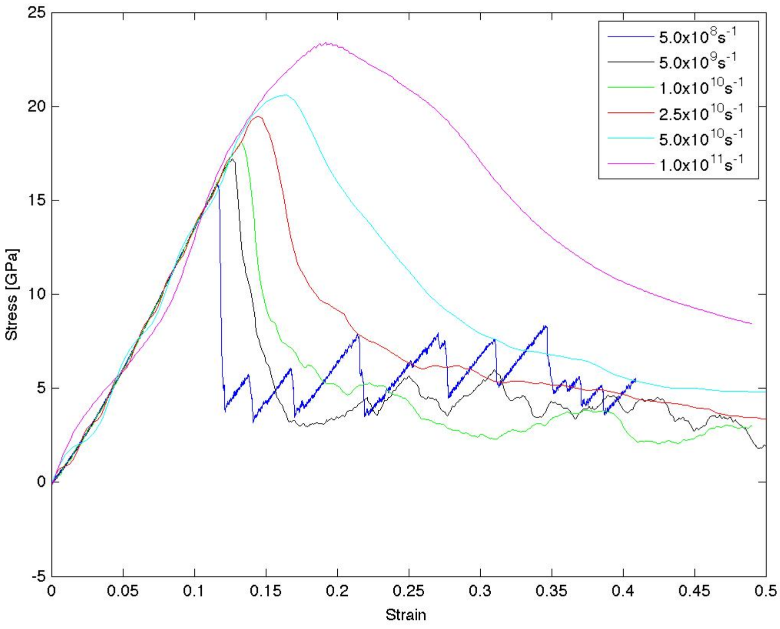

Figure 11: Stress-strain curves for Ni nanorod under tension with different strain rates

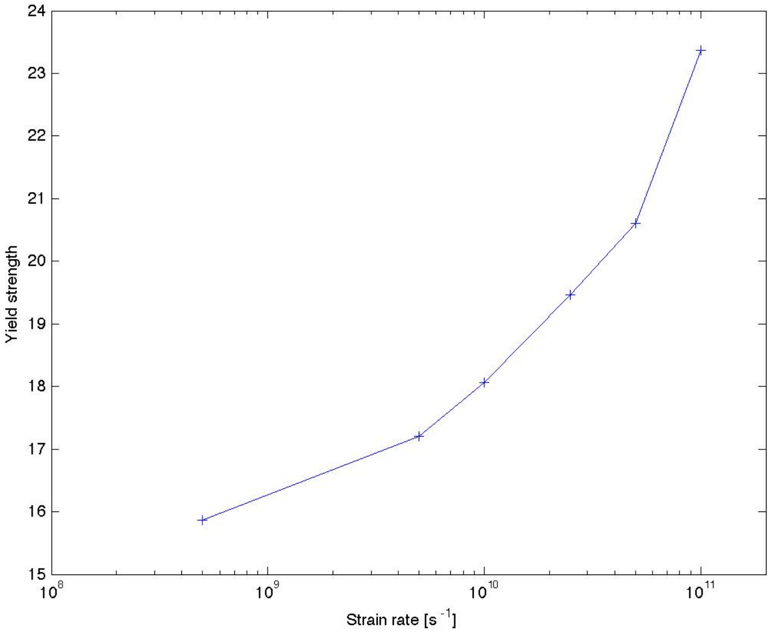

Figure 12: Yield strength for different tensile strain rates in a semilog plot

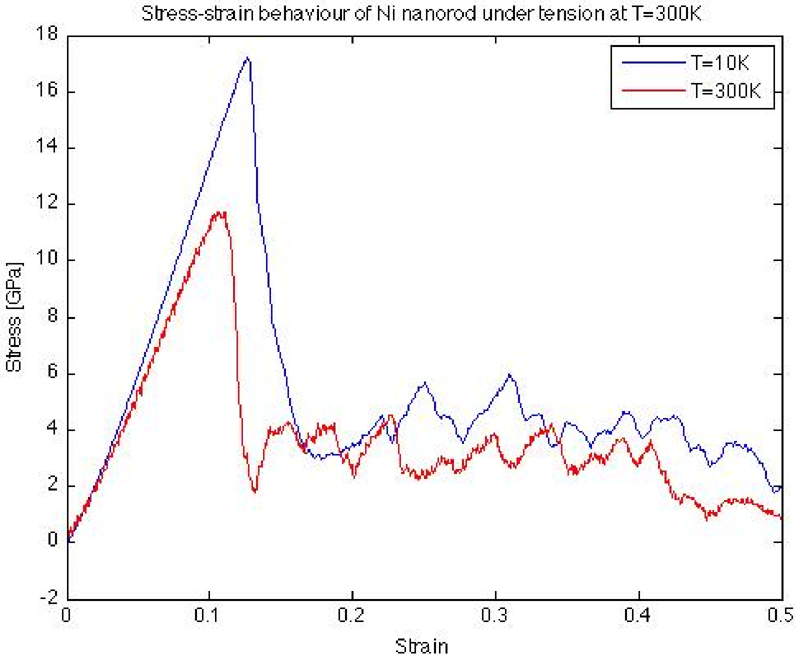

Figure 13: Stress-strain curves for Ni nanorod under tension at T = 10 K and T = 300 K

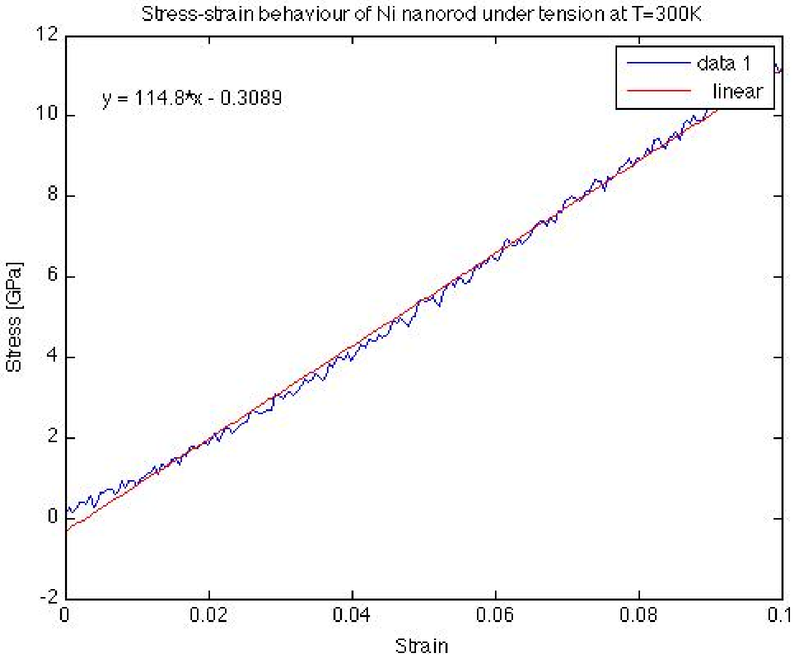

Figure 14: Elastic portion of stress-strain curve for Ni nanorod under tension at T = 300 K

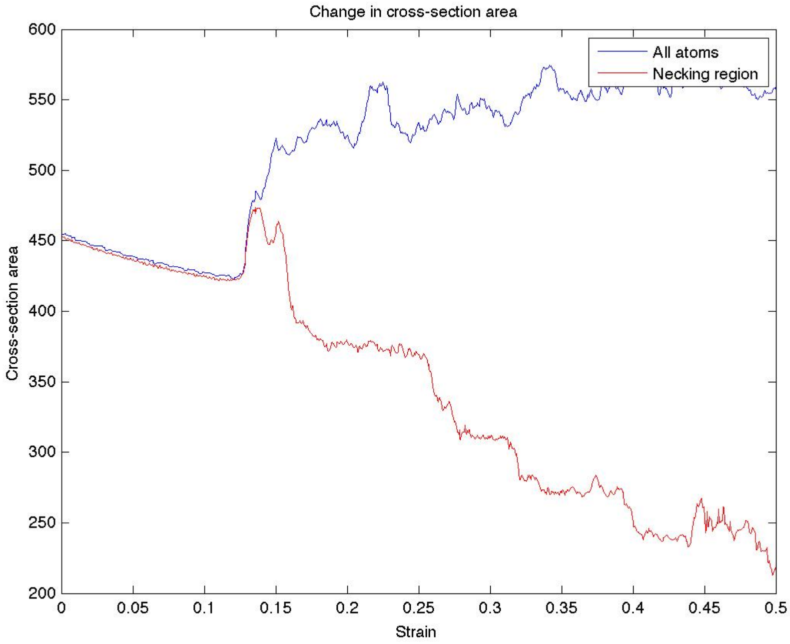

Figure 15: Change in the computed cross-section for the whole box (blue curve) and the region where necking occurs(red line)

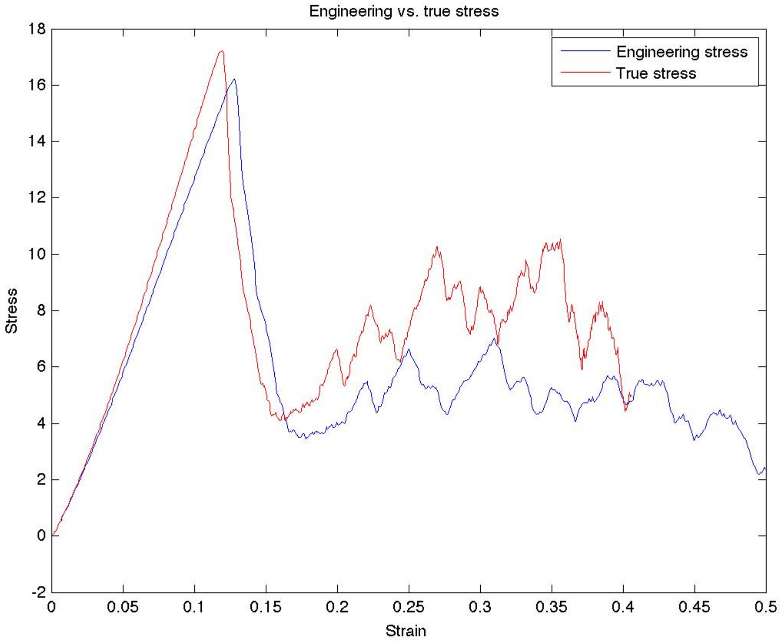

Figure 16: True stress-strain (red curve) compared to engineering stress-strain (blue curve)

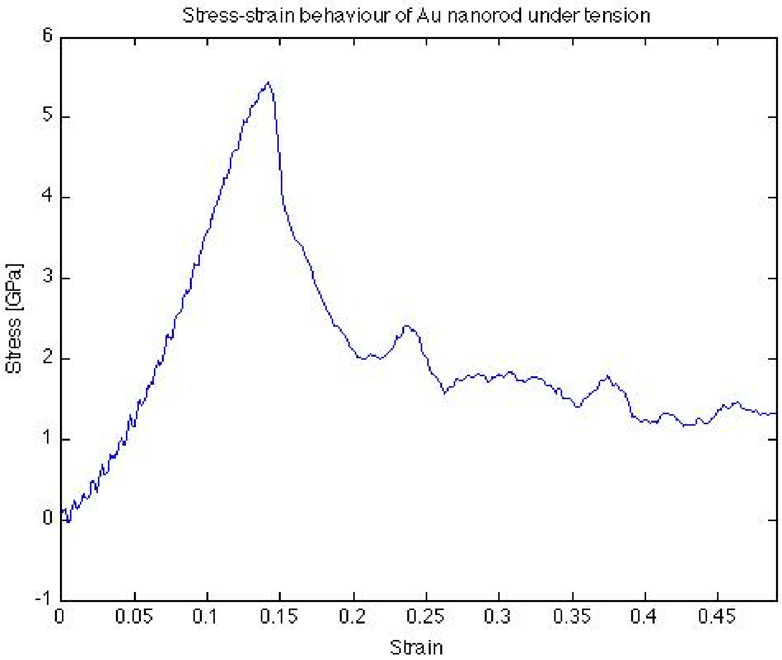

Figure 17: Stress-strain curve for Au nanorod under tension

Figure 16 shows the true stress-strain and the engineering stress-strain compared in the same plot. It can be seen that the elastic modulus is higher, that plastic deformation occurs at lower strain and that the stress increases again after yielding has occured for the true stress-strain.

3.6 Elastic properties of other elements

As in section 3.1, tensile tests have been done by using the EAM-potential but with different elements than nickel. Figure 17 and 18 shows the engineering stress-strain relation for gold, with an estimated elastic modulus of $E = 47.3$ GPa. The stress-strain relation for copper were also calculated, and are shown in figure 19 and 20, with an estimated elastic modulus of $E = 80.1$ GPa. The stress-strain relations shows the same kind of behaviour as nickel, just with other elastic properties.

4 Discussion

4.1 Deformation

From the stress-strain curve in figure 1 for a nickel nanowire under tension, one can see that the deformation is elastic until an engineering strain of about 12 % is reached, which is also shown in figure 2. At this point there is a rapid decrease in the stress, indicating that the nanowire yields at this point, and that further deformation is irreversible. From around 20 % deformation and onwards, the stress goes up and down in a zig-zag pattern. The zig-zag pattern is due to nucleation, transformation and junction of dislocations in the

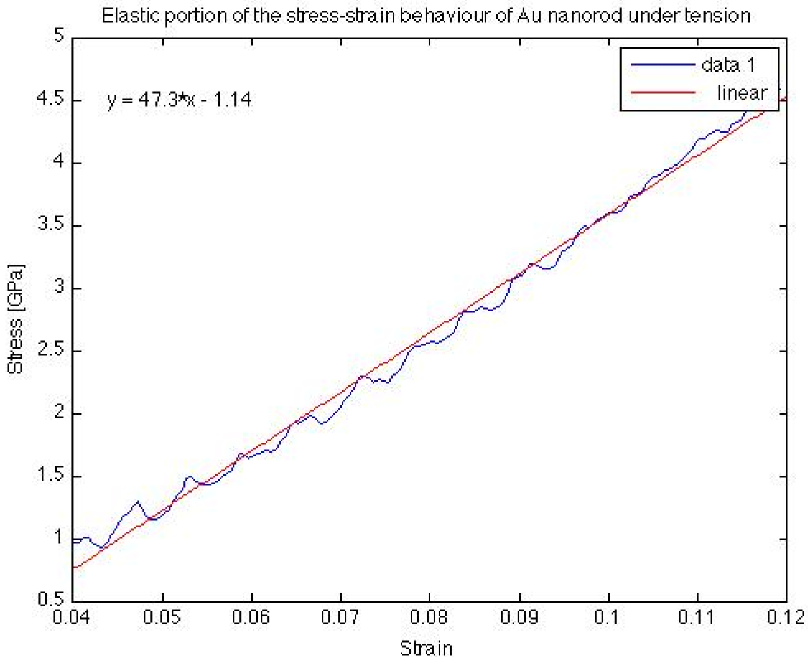

Figure 18: Elastic portion of the stress-strain curve for Au nanorod under tension

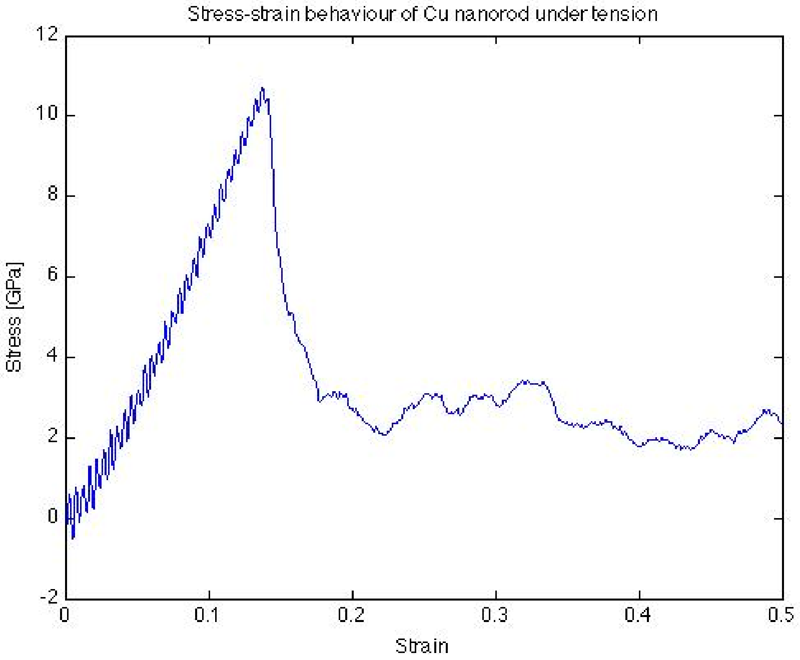

Figure 19: Stress-strain curve for Cu nanorod under tension

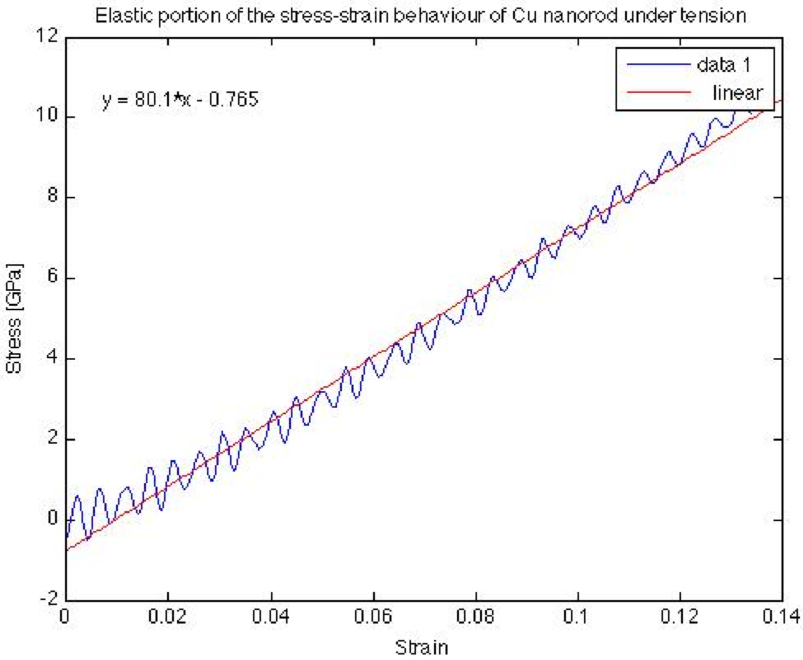

Figure 20: Elastic portion of the stress-strain curve for Cu nanorod under tension

nanowire [4]. The mean value of the stress in the range from 20 % to 45 % is fluctuating about an approximately constant value, with a small drop close to 50 %, which is the end of the simulation. The nanowire does not fracture as the stress does not return to a zero value. The mechanical behaviour of the nanowire is different from that of a bulk material, as the rapid decrease in stress after yield is not common at a larger scale [5]. Therefore, the yield strength is taken as the maximum stress observed, and not the intersection with the extrapolated elastic curve offset by 0.2 %.

The stress strain-curve for the same nanowire under compression is displayed in figure 3. Initially, the stress increases linearly with strain before nonlinear deformation starts at around 2 % compression. The slope then decreases until it becomes constant, before a sharp drop occurs. From this point, the stress-strain behaviour shows a much more pronounced zig-zag pattern. The sharp drops indicates offset of slip deformation. At the end, close to 30 %, the stress increases and reaches peak values above that of the elastic yield stress. The wire does not however fracture.

Figure 5 and 6 shows the onset of slip and twinning deformation for tension and compression respectively. For tension, one can observe necking near the middle of the wire, however it does not fracture as was already shown by the stress-strain curve. At the end of the compression simulation, it looks like the wire conforms into a more or less ordered state, somehow sheared from the inital conformation.

4.2 Size effects

The mechanical properties of materials is dependent on the length scale of the objects, and behaves quite differently on the nanoscale as have already been discussed. Therefore it was interesting to see how the stress-strain behaviour is changed when the length of the wire is increased. Figure 7 and figure 8 therefore compares the two different nanowires. It can be seen that the elastic modulus and the yield strength is practically independent when increasing the length from 6.94 nm to 13.88 nm and 20.82 nm, for both tension and compression. This seems reasonable, as there are no defects introduced in these structures. For real physical structures, a larger rod would have a higher probability of having defects, which would initiate fracture propagation. In the plastic regime however, the length of the wire does matter. As could be seen from figure 9, the two larger nanowire actually fractures, opposite to the shortest one. This could also be seen from the stress-strain behaviour. From the compression tests, it is difficult to draw conclusions, but it appears that the shorter nanowire is harder than the longer.

4.3 Engineering strain-rate

Previous work has shown that the stress-strain relation is not independent of the strain rate [1]. This is confirmed by figure 11. In the elastic part, the curves are more or less overlapping, although they are not perfect linear. Compared with the previous work of Wen *et. al.*, it may be assumed that Young's modulus is not dependent on the strain-rate [1]. As can be seen from the plot, the yield strength is however higher when a large strain-rate is applied than for a low one. It ranges between 15.9 GPa and 23.4 GPa for the applied strain rates. The lowest value of these is significantly higher than that reported for bulk nickel, about 0.14 GPa [1]. This can be explained by the fact that the simulated nanowire is defect-free, which is not the case for real materials. Defects, such as dislocations and impurities, facilitates deformation.

Also, it can be seen that the there is a more significant decrease in stress after the yielding point at lower strain rates. Figure 12 shows the dependancy between yield strength and strain rate; the dependancy is not so strong at lower strain rates, but increase rapidly with higher rates. It has been suggested that at very high loading rates, the nickel nanowire transforms into an amorphous state [4]. At lower strain-rates, the atoms have more time to relax into equilibrium when old atomic bonds are broken and new ones are formed. Thus, dislocations moves easier, which facilitates plastic deformation. At higher strain-rates, the dislocations have a higher restriction against moving in the material, leading to higher yield strengths.

4.4 Temperature dependance

The stress strain relation for the nickel nanowire at two different temperatures, namely T = 10K and T = 300K are shown in figure 13. Both the elastic modulus and the yield strength is lower at higher temperatures. This corresponds well with previously published results for nickel nanowires, where it was shown that both quantities decreased linearly with increasing temperature [4]. The reason for this is that the equilibrium distance σ between two atoms, where the system have a minimal potential energy, increases with increased temperature. Because thermal fluctuations contributes to the sum of molecular forces, the energy landscape is tilted towards higher separation values. Increasing the thermal force results in weaker bonds between atoms, and less energy is required to break them. Thus, the material behaves softer at higher temperatures. Also, nucleation rate of dislocations increase with increasing temperatures, so the nanowire enters the plastic region at lower stresses.

4.5 True stress-strain behaviour

Usually, when measuring mechanical properties of materials, one calculates the engineering stress and engineering rate. This means that one assumes that the cross-sectional area of the material is constant. However, this is in fact not a good approximation. As we have seen figure 5 and 9, necking occurs during tensile deformation, thus the cross-sectional area have a distribution along the z-axis. This is indeed confirmed by looking at figure 15, which shows the cross-sectional area of the whole box compared to that of the necking region. In the elastic regime, these two-values is more or less overlapping, as no necking occurs. However, after yielding, the calculated area increases for the whole box due to the fact that the nanowire exhibits a non-uniform rectangular shape (due to formation of slip-planes), while the area in the necking region decreases as expected. The non-uniform area distribution, means that the stress also is not uniformly distributed in the nanowire. Since stress is defined as load per cross-sectional area, the stress concentration is highest in the necking region. It may therefore be interesting to investigate the true stress-strain behaviour, as this gives us more correct information about the deformation process in the area which are most interesting from a mechanistic point of view, namely the necking region as this is were the nanowire will fracture.

Figure 16 compares the stress-strain behaviour when true stress is calculated instead of engineering stress. It shows that both the elastic modulus and yield stress is higher when using true stress, due to the more correct method of calculating true strain. Since necking occurs, the stress in the plastic regime is higher than what would be calculated using engineering stress.

4.6 Mechanical behaviour of Ni, Cu and Au nanowires

From the simulation results, one can extract information about the Young's modulus and the yield strength for the nickel, copper and gold nanowires under tension and compare the results when all other parameters are kept constant. The results are collected in table 1 and shows that nickel nanorods have superior mechanical properties compared copper and gold, which are softer and yields plastically at a lower stress. The values of Young's modulus listed for the nanowires are lower than that of the bulk properties, which have been reported to be 199.5 GPa, 117.2 GPa and 74.5 GPa for nickel, copper and gold respectively [6]. There may be several reasons why the values are lower than for the bulk material. First, it may be that the EAM model used is not estimating real physical atoms with a sufficient accuracy. Also, nanostructures have a significantly higher surface/volume ratio than bulk material. The surface atoms have fewer nearest neighbour atoms than bulk atoms, thus they have a weaker bond to the material. Finally, the simulated structures are defect-free, which are far from the truth in real bulk materials. Thus, the yield strength may not be that accurate estimate using these kinds of simulations.

Element	Young's modulus [GPa]	Yield strength [GPa
Nickel	142.2	17.0
Copper	80.1	10.6
Gold	47.3	5.4

Table 1: Comparison of the mechanical properties of nanowires of three different elements with all other parameters kept constant

5 Conclusion

Molecular dynamics simulations have been used to examine the mechanical properties of nanowires with different elemental composition, and the effect of size, temperature and strain-rate. In addition, the true stress-strain relation was compared to the engineering stress. The nanowires examined showed a very sharp transition between elastic and plastic deformation for both tension and compression. The effect of size had practically no impact in the elastic regime, but showed different behaviour in the plastic regime due to a difference in the surface/volume ratio. Structures with higher surface/volume ratios displayed fracture at lower strains. Furthermore, the elastic modulus showed no depence upon strain-rate, while the yield strength increased with increasing strain rates. Both quantities decreased with increasing temperature, due to a larger thermal force.

True stress-strain behaviour gives a more realistic result of the mechanical behaviour in the plastic regime, because the change in cross-sectional area due to necking is taken into account. Finally, the elastic modulus and yield strength was both shown to be lower for a copper nanowire than nickel, but higher than for a gold nanowire. These trends agree well with observed experimental values.

Mechanics at the nanoscale is different from mechanics at the macro-scale, mostly because of a higher surface/volume ratio and smaller grain sizes. Molecular dynamics is a powerful tool to investigate nanomechanical behaviour. One has to be careful however, because materials used in simulations does not always represent the real physical world, especially when considering defects and impurities.

References

[1] Y. H. Wen, Z. Z. Zhu, and R. Z. Zhu, “Molecular dynamics study of the mechanical behavior of nickel nanowire: Strain rate effects,” *Computational Materials Science*, vol. 41, no. 4, pp. 553–560, 2008.

[2] S. M. Foiles, M. I. Baskes, and M. S. Daw, “Embedded-atom-method functions for the fcc metals cu, ag, au, ni, pd, pt, and their alloys,” *Phys. Rev. B*, vol. 33, pp. 7983–7991, Jun 1986.

[3] M. S. Daw and M. I. Baskes, “Embedded-atom method: Derivation and application to impurities, surfaces, and other defects in metals,” *Phys. Rev. B*, vol. 29, pp. 6443–6453, Jun 1984.

[4] A. R. Setoodeh, H. Attariani, and M. Khosrownejad, “Nickel nanowires under uniaxial loads: A molecular dynamics simulation study,” *Computational Materials Science*, vol. 44, no. 2, pp. 378–384, 2008.

[5] J. Schiøtz, F. D. Di Tolla, and K. W. Jacobsen, “Softening of nanocrystalline metals at very small grain sizes,” *Nature*, vol. 391, pp. 561–563, 1998.

[6] R. W. Hertzberg, *Deformation and Fracture Mechanics of Engineering Materials.* Wiley, New York, 1983.